

SPECTROSCOPIC OBSERVATIONS OF SN 2012FR: A LUMINOUS NORMAL TYPE IA SUPERNOVA WITH EARLY HIGH VELOCITY FEATURES AND LATE VELOCITY PLATEAU

M. J. CHILDRESS^{1,2,†}, R. A. SCALZO^{1,2}, S. A. SIM^{1,2,3}, B. E. TUCKER¹, F. YUAN^{1,2}, B. P. SCHMIDT^{1,2}, S. B. CENKO⁴, J. M. SILVERMAN⁵, C. CONTRERAS⁶, E. Y. HSIAO⁶, M. PHILLIPS⁶, N. MORRELL⁶, S. W. JHA⁷, C. MCCULLY⁷, A. V. FILIPPENKO⁴, J. P. ANDERSON⁸, S. BENETTI⁹, F. BUFANO¹⁰, T. DE JAGER⁸, F. FORSTER⁸, A. GAL-YAM¹¹, L. LE GUILLOU¹², K. MAGUIRE¹³, J. MAUND³, P. A. MAZZALI^{14,9,15}, G. PIGNATA¹⁰, S. SMARTT³, J. SPYROMILIO¹⁶, M. SULLIVAN¹⁷, F. TADDIA¹⁸, S. VALENTI^{19,20}, D. D. R. BAYLISS¹, M. BESSELL¹, D. J. CARSON²¹, K. I. CLUBB⁴, C. DE BURGH-DAY²², T. D. DESJARDINS²³, J. J. FANG²⁴, O. D. FOX⁴, E. L. GATES²⁴, I-T. HO²⁵, S. KELLER¹, P. L. KELLY⁴, C. LIDMAN²⁶, N. S. LOARING²⁷, J. R. MOULD²⁸, M. OWERS²⁶, S. OZBILGEN², L. PEI²¹, M. B. PRACY²⁹, B. E. SCHAEFER³⁰, N. SCOTT²⁸, M. STRITZINGER³¹, F. P. A. VOGT¹, G. ZHOU¹

Draft version February 14, 2013

ABSTRACT

We present spectroscopic observations of the Type Ia supernova SN 2012fr, comprising 50 optical spectra, of which 29 were obtained before maximum light, and five near infrared spectra. At early times SN 2012fr shows clear evidence of a high velocity feature (HVF) in the Si II λ 6355 which can be cleanly decoupled from the lower velocity “photospheric” component. This Si II λ 6355 HVF fades by phase -5, then the photospheric component exhibits a very narrow velocity width and remains at a nearly constant velocity of $v \sim 12,000 \text{ km s}^{-1}$ until at least 5 weeks post-maximum. The Ca II IR triplet exhibits similar evidence for both a photospheric component at $v \sim 12,000 \text{ km s}^{-1}$ with narrow line width and long velocity plateau, as well as a high velocity component beginning at $v \sim 32,000 \text{ km s}^{-1}$ two weeks before maximum. SN 2012fr resides on the border between the “shallow silicon” and “core-normal” subclasses in the Branch et al. (2009) classification scheme, and on the border between normal and “high-velocity” SNe Ia in the Wang et al. (2009a) system. Though it is a clear member of the “low velocity gradient” (LVG – Benetti et al. 2005) group of SNe Ia and exhibits a very slow light curve decline, it shows key dissimilarities with the overluminous SN 1991T or SN 1999aa subclasses of SNe Ia. SN 2012fr represents a well observed SN Ia at the luminous end of the normal SN Ia distribution, and a key transitional event between nominal spectroscopic subclasses of SNe Ia.

Subject headings: supernovae: individual: SN 2012fr — supernovae: general — galaxies: individual: NGC 1365

¹ Research School of Astronomy and Astrophysics, The Australian National University, Mount Stromlo Observatory, Cotter Road, Weston Creek ACT 2611, Australia

² ARC Centre of Excellence for All-sky Astrophysics (CAASTRO)

³ Astrophysics Research Centre, School of Mathematics and Physics, Queen’s University Belfast, Belfast BT7 1NN, UK

⁴ Department of Astronomy, University of California, Berkeley, CA 94720-3411, USA

⁵ Department of Astronomy, University of Texas, Austin, TX 78712-0259, USA

⁶ Las Campanas Observatory, Carnegie Observatories, Casilla 601, La Serena, Chile

⁷ Department of Physics and Astronomy, Rutgers the State University of New Jersey, 136 Frelinghuysen Road, Piscataway, NJ 08854, USA

⁸ Departamento de Astronomía, Universidad de Chile, Casilla 36-D, Santiago, Chile

⁹ INAF Osservatorio Astronomico di Padova, Vicolo dell’Osservatorio 5, 35122 Padova, Italy

¹⁰ Departamento de Ciencias Fisicas, Universidad Andres Bello, Avda. Republica 252, Santiago, Chile

¹¹ Department of Particle Physics and Astrophysics, The Weizmann Institute of Science, Rehovot 76100, Israel

¹² UPMC Univ. Paris 06, UMR 7585, Laboratoire de Physique Nucleaire et des Hautes Energies (LPNHE), 75005 Paris, France

¹³ Department of Physics (Astrophysics), University of Oxford, DWB, Keble Road, Oxford OX1 3RH, UK

¹⁴ Astrophysics Research Institute, Liverpool John Moores University, Egerton Wharf, Birkenhead, CH41 1LD, UK

¹⁵ Max-Planck-Institut für Astrophysik, Karl-Schwarzschild str. 1, 85748 Garching, Germany

¹⁶ European Southern Observatory, Karl-Schwarzschild str 2,

Garching D-85748, Germany

¹⁷ School of Physics and Astronomy, University of Southampton, Southampton SO17 1BJ, UK

¹⁸ The Oskar Klein Centre, Department of Astronomy, AlbaNova, Stockholm University, 10691 Stockholm, Sweden

¹⁹ Las Cumbres Observatory Global Telescope Network, 6740 Cortona Dr., Suite 102, Goleta, CA 93117, USA

²⁰ Department of Physics, University of California, Santa Barbara, Broida Hall, Mail Code 9530, Santa Barbara, CA 93106-9530, USA

²¹ Department of Physics and Astronomy, University of California, Irvine, CA 92697-4575, USA

²² School of Physics, University of Melbourne, Parkville, VIC 3010 Australia

²³ Department of Physics and Astronomy, The University of Western Ontario, London, ON N6A 3K7 Canada

²⁴ University of California Observatories/Lick Observatory, University of California, Santa Cruz, CA 95064, USA

²⁵ Institute for Astronomy, University of Hawaii, 2680 Woodlawn Drive, Honolulu, HI 96822, USA

²⁶ Australian Astronomical Observatory, PO Box 915, North Ryde, NSW 1670, Australia

²⁷ South African Astronomical Observatory (SAAO), P.O. Box 9, Observatory 7935, South Africa

²⁸ Centre for Astrophysics & Supercomputing, Swinburne University of Technology, PO Box 218, Hawthorn, VIC 3122, Australia

²⁹ Sydney Institute for Astronomy, School of Physics, University of Sydney, NSW 2006, Australia

³⁰ Department of Physics and Astronomy, Louisiana State University, Baton Rouge, Louisiana, 70803, USA

³¹ Department of Physics and Astronomy, Aarhus University, Ny Munkegade 120, DK-8000 Aarhus C, Denmark

[†] E-mail: mjc@mso.anu.edu.au

1. INTRODUCTION

Type Ia supernovae (SNe Ia) are critical cosmological tools for measuring the expansion history of the Universe (Riess et al. 1998; Perlmutter et al. 1999), yet much remains unknown about the nature of these enlightening explosions. Their luminosities show low intrinsic dispersion (~ 0.35 mag) and they generally obey a scaling of their absolute luminosity with the width of their optical light curve (Phillips 1993; Phillips et al. 1999), about which the brightness dispersion is even lower. The width-luminosity relationship appears to be driven by the amount of radioactive ^{56}Ni produced in the explosion and the opacity (Pinto & Eastman 2000; Mazzali et al. 2001, 2007), but the progenitor mechanism driving these properties remains uncertain. Whether SNe Ia represent a unified class of objects with a common physical origin or result from multiple progenitor channels has yet to be determined, and is a critical question for the continued use of SNe Ia in cosmology.

Optical spectroscopy of SNe Ia can provide vital insight into the question of SN Ia diversity. Large samples of SN Ia spectra have been made publicly available (e.g. Matheson et al. 2008; Blondin et al. 2012; Silverman et al. 2012b; Yaron & Gal-Yam 2012), and investigations of spectroscopic sub-classification of SNe Ia have been a vigorous area of study (Benetti et al. 2005; Branch et al. 2009; Wang et al. 2009a; Silverman et al. 2012a). While a rigorous accounting of the diversity of SNe Ia is crucial for understanding the source of their luminosity dispersion, individual cases of well-studied SNe Ia (e.g. Stanishev et al. 2007; Wang et al. 2009b; Foley et al. 2012; Silverman et al. 2012c) can yield key insights into the nature of the explosions themselves.

In this work we focus on the optical spectroscopy of SN 2012fr, a SN Ia which was discovered on 27-Oct-2012 in the nearby barred spiral NGC 1365. Shortly after its discovery we initiated a rigorous photometric and spectroscopic followup program for SN 2012fr. Optical photometry were presented in Contreras et al. (2013 – hereafter Paper I), where we showed SN 2012fr has a normal light curve for an SN Ia. This paper presents the optical spectra of SN 2012fr, while Hsiao et al. (2013 – Paper III) will present NIR spectra and Tucker et al. (2013 – Paper IV) will analyze constraints on the progenitor from pre-explosion imaging and very early photometry.

This paper is organized as follows. In Section 2 we present the observational data. Section 3 focuses on the Si II $\lambda 6355$ line, and characterizes both the high-velocity features observed at early times and the long velocity plateau observed at late times. Other absorption features of particular note for SN 2012fr – including narrow Na I D, unburned carbon, the Ca II IR triplet, and Fe-group elements – are inspected in Section 4. We address the spectroscopic “sub-classification” of SN 2012fr in the context of modern classification schemes in Section 5. We then discuss implications of our observational results in Section 6 and present concluding remarks in Section 7.

2. SPECTROSCOPIC OBSERVATIONS

SN 2012fr was discovered on 2012-Oct-27 UT by Klotz et al. (2012) at $\alpha = 03:33:36.274$, $\delta = -36:07:34.46$ in the nearby barred spiral galaxy NGC 1365, then shortly thereafter classified as a Type Ia supernova

(Childress et al. 2012; Buil 2012). Extensive photometric coverage presented in Paper I showed SN 2012fr to reach a peak brightness of $m_B = 12.0$ on 2012-Nov-12.04 with a decline rate of $\Delta m_{15}(B) = 0.80$. Given the nominal distance modulus to NGC 1365 of $\mu = 31.3$ (Silbermann et al. 1999; Freedman et al. 2001), this implies a peak luminosity of $M_B = -19.3$, placing it in firm agreement with the Phillips (1993) relation.

Spectroscopy of SN 2012fr was collected from multiple sources. The two main sources of spectra were the Wide Field Spectrograph (WiFeS – Dopita et al. 2007, 2010) on the Australian National University (ANU) 2.3m telescope at Siding Spring Observatory in northern New South Wales, Australia, and the Public ESO Spectroscopic Survey of Transient Objects (PESSTO) utilizing the 3.6m New Technology Telescope (NTT) at La Silla, Chile.

WiFeS spectra were obtained using the B3000 and R3000 gratings, providing wavelength coverage from 3500 Å to 9600 Å with a resolution of 1.5 Å and 2.5 Å (all reported instrument resolutions are FWHM) on the blue and red channels, respectively. Data cubes for WiFeS observations were produced using the PyWiFeS software¹ (Childress et al. 2013, in prep.). Spectra of the SN were extracted from final data cubes using a PSF-weighted extraction technique with a simple symmetric Gaussian PSF, and the width of this Gaussian was measured directly from the data cube. We found this method to produce flux measurements consistent with a simple aperture extraction method, but with improved signal-to-noise. Background subtraction was performed by calculating the median background spectrum across all spaxels outside a distance from the SN equal to about three times the seeing (which was typically 1.5-2"). Due to the negligible galaxy background and good spatial flat-fielding from the PyWiFeS pipeline, this technique produced favorable subtraction of the sky background from the WiFeS spectra for SN 2012fr.

A major component of our observing campaign was a series of optical and near-infrared spectra obtained as part of the PESSTO (Smartt et al., 2013, in prep.)² survey using the NTT-3.6m telescope in La Silla, Chile. Optical spectra from PESSTO were obtained with EFOSC2 (Buzzoni et al. 1984) using the Gr11 and Gr16 grisms, which both have a resolution of 16Å. NIR spectra were obtained with SOFI (Moorwood et al. 1998) using the GB and GR grisms, which give respective resolutions of 14Å and 21Å. SOFI observations were dithered to facilitate sky background subtraction. EFOSC and SOFI spectra were both reduced using the PESSTO pipeline developed by S. Valenti, which is a custom-built python/pyraf package that performs all standard spectroscopic reduction steps including preprocessing, wavelength and flux calibration, and final spectrum extraction. This paper marks the data release of PESSTO optical and NIR spectra for SN 2012fr taken in 2012. Continued observations of SN 2012fr in 2013 are ongoing as part of the PESSTO operations and will be presented in a future PESSTO paper.

Additional spectra of SN 2012fr were obtained with

¹ <http://www.mso.anu.edu.au/pywifes/>

² <http://www.pessto.org>

the Robert Stobie Spectrograph on the South African Large Telescope (SALT), the Grating Spectrograph on the South African Astronomical Observatory (SAAO) 1.9m telescope, and the Kast Double Spectrograph (Miller & Stone 1993) on the Shane 3-m telescope at Lick Observatory. SALT/RSS observations were obtained with a 900 l/mm VPH grating at three tilt angles to cover the range from 3480-9030 Å. The 1.5" longslit yielded a resolution of approximately 6Å. Initial processing of the SALT data utilized the SALT science pipeline PySALT³ (Crawford et al. 2010). SAAO-1.9m observations used the 300 l/mm grating (#7) at a grating angle of 17.5 corresponding to a central wavelength of 5400 Å and an approximate wavelength range of 3500-7300Å and a resolution of 5Å.

Kast observations employed the 600 l/mm grating on the blue arm, which blazes at 4310Å and provides wavelength coverage from 3500-5600Å with a resolution of 6.6Å. Different observers used different gratings on the Kast red arm, including the 300 l/mm grating blazed at 7500Å and covering 5500-10300Å with a resolution of 11Å, the 600 l/mm grating blazed at 7000Å and covering 5600-8200Å with 5.5Å resolution, and the 830 l/mm grating blazed at 6500Å and covering 5600-7440Å with 4Å resolution.

We obtained a high-resolution optical spectrum of SN 2012fr with the High Resolution Echelle Spectrometer (HIRES; Vogt et al. 1994) on the 10 m Keck I telescope with the blue cross-disperser ("HIRESb") on 2012 Oct 29.45. We used the C2 decker (i.e., the 1.15" slit), providing coverage from the atmospheric cutoff to $\lambda = 5960$ Å with a resolution of 37000.

A full table of our optical spectra is given in Table 1, and a representative plot of our spectral time series is shown in Figure 1. Table 2 lists the SOFI NIR spectroscopy observation dates, and the SOFI spectra are plotted in Figure 2. At the earliest epochs of SN 2012fr, our observing strategy was to request spectra from multiple sources worldwide. This resulted in multiple spectra in the same night (often separated by 0.3-0.5 days) on some occasions, but consistently resulted in at least one spectrum every night until nearly two weeks after maximum light. On nights with extremely poor seeing ($>3''$) at Siding Spring, some WiFeS observers chose to observe SN 2012fr multiple times due to inability to observe their own fainter targets. Upon publication of this paper we will make all our optical spectra publicly available via the WISEREP (Yaron & Gal-Yam 2012) SN spectroscopy repository.

3. EVOLUTION OF THE Si II λ 6355 LINE

The Si II λ 6355 line is among the most prominent features in SN Ia spectra. Both its characteristics at maximum light (e.g. Nugent et al. 1995) and its evolution in time (e.g. Benetti et al. 2005) have been key tools in characterizing SN Ia diversity. Additionally, the properties of this line in combination with behavior of other lines ("spectral indicators") have been used to identify potential subclasses of SNe Ia (e.g. Benetti et al. 2005; Bongard et al. 2006; Branch et al. 2009; Silverman et al.

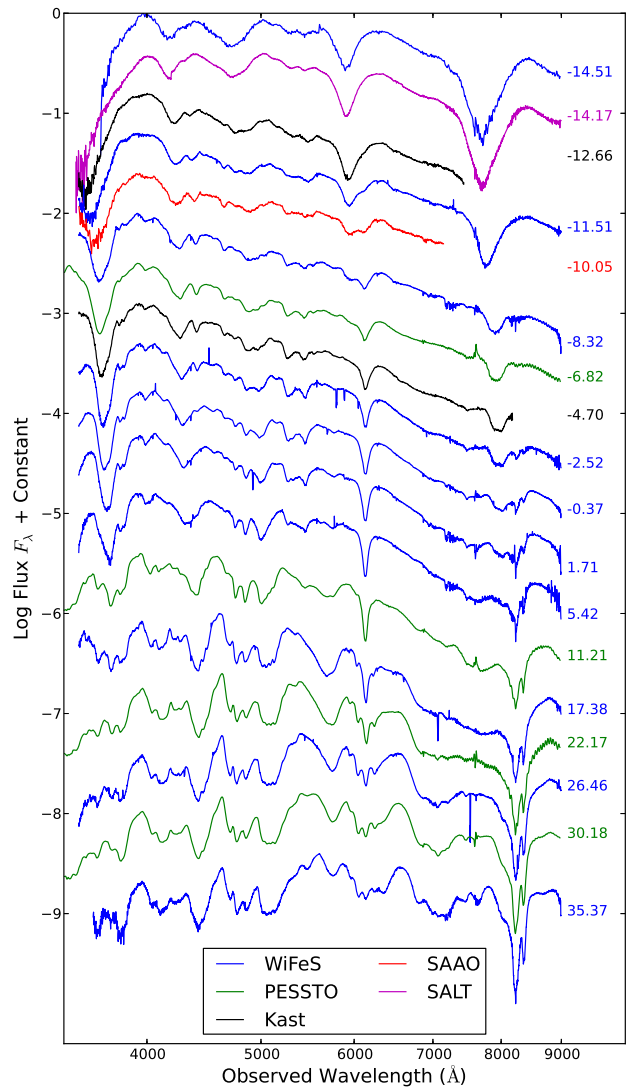


Figure 1. Representative sample of SN 2012fr spectra, color coded by instrument, labeled by phase with respect to B -band maximum light.

2012a; Blondin et al. 2012).

For SN 2012fr, the evolution of the Si II λ 6355 has three key features of note: (1) the velocity width of the line (and indeed other lines, see Section 4) is extremely narrow, starting about a week after maximum; (2) early spectra show clear signature of a double-profiled Si II λ 6355, indicating a layer of ejected material at higher velocities than the nominal photospheric layer; and (3) the velocity of the photospheric component remains constant (to within ~ 200 km s⁻¹) to at least ~ 40 days after maximum.

The clear detections of both the high-velocity layer and the constant photospheric velocity are facilitated by the extremely narrow velocity width of the photospheric absorption lines in SN 2012fr. In Figure 3 we show the width of the Si II λ 6355 for SN 2012fr viewed in velocity space, compared to that of SN 2005hj (Quimby et al. 2007), SN 1994D (from Blondin et al. 2012), and SN 2002bo (Benetti et al. 2004). SN 2012fr has a narrower Si II λ 6355 than the other SNe Ia, except

³ <http://pysalt.salt.ac.za>

Table 1
Optical Spectroscopy Observation Log

UT Date	Phase ^a (days)	Telescope / Instrument	Exposure Time (s)	Wavelength Range (Å)	Observers ^b
2012-Oct-28.53	-14.51	ANU-2.3m / WiFeS	900	3500-9550	GZ, DB
2012-Oct-28.87	-14.17	SALT / RSS	1200	3480-9030	SJ, CM1
2012-Oct-29.45	-13.59	Keck-I / HIRES	1200	3500-5960	BZ, MJ, SX, BK
2012-Oct-30.38	-12.66	Lick-3m / Kast	2000	3500-7440	CM2, BZ
2012-Oct-30.51	-12.53	ANU-2.3m / WiFeS	1200	3500-9550	GZ, DB
2012-Oct-31.53	-11.51	ANU-2.3m / WiFeS	1200	3500-9550	GZ, DB
2012-Nov-01.59	-10.45	ANU-2.3m / WiFeS	1200	3500-5700 ^c	MB, SK
2012-Nov-01.99	-10.05	SAAO-1.9m / GS	900	3500-7150	NSL
2012-Nov-02.48	-9.56	ANU-2.3m / WiFeS	900	3500-9550	MB, SK
2012-Nov-02.69	-9.35	ANU-2.3m / WiFeS	900	3500-9550	MB, SK
2012-Nov-03.05	-8.99	SAAO-1.9m / GS	900	3500-7150	NSL
2012-Nov-03.57	-8.47	ANU-2.3m / WiFeS	900	3500-9550	MB, SK
2012-Nov-03.72	-8.32	ANU-2.3m / WiFeS	900	3500-9550	MB, SK
2012-Nov-04.07	-7.97	SAAO-1.9m / GS	900	3500-7150	NSL
2012-Nov-04.34	-7.70	Lick-3m / Kast	600	3500-8220	EG
2012-Nov-04.50	-7.54	ANU-2.3m / WiFeS	900	3500-9550	MB, SK
2012-Nov-05.22	-6.82	NTT-3.6m / EFOSC	100	3360-10000	PESSTO
2012-Nov-05.37	-6.67	Lick-3m / Kast	600	3500-8220	EG
2012-Nov-05.61	-6.43	ANU-2.3m / WiFeS	900	3500-9550	MB, SK
2012-Nov-06.38	-5.66	Lick-3m / Kast	180	3500-10300	SBC, PK
2012-Nov-07.27	-4.77	NTT-3.6m / EFOSC	100	3360-10000	PESSTO
2012-Nov-07.34	-4.70	Lick-3m / Kast	180	3500-8180	LP, DC
2012-Nov-08.24	-3.80	NTT-3.6m / EFOSC	100	3360-10000	PESSTO
2012-Nov-08.34	-3.70	Lick-3m / Kast	180	3500-8180	LP, DC
2012-Nov-09.52	-2.52	ANU-2.3m / WiFeS	900	3500-9550	FV
2012-Nov-09.62	-2.42	ANU-2.3m / WiFeS	900	3500-9550	FV
2012-Nov-10.57	-1.47	ANU-2.3m / WiFeS	700	3500-9550	FV
2012-Nov-10.70	-1.34	ANU-2.3m / WiFeS	900	3500-9550	FV
2012-Nov-11.67	-0.37	ANU-2.3m / WiFeS	900	3500-9550	FV
2012-Nov-12.38	+0.34	Lick-3m / Kast	180	3500-8220	TD, JF
2012-Nov-12.74	+0.70	ANU-2.3m / WiFeS	600	3500-9550	MO, MP
2012-Nov-13.26	+1.22	NTT-3.6m / EFOSC	100	3360-10000	PESSTO
2012-Nov-13.75	+1.71	ANU-2.3m / WiFeS	600	3500-9550	MO, MP
2012-Nov-14.32	+2.28	Lick-3m / Kast	300	3500-10300	KC, OF
2012-Nov-15.22	+3.18	NTT-3.6m / EFOSC	100	3360-10000	PESSTO
2012-Nov-16.51	+4.47	ANU-2.3m / WiFeS	600	3500-9550	NS
2012-Nov-17.46	+5.42	ANU-2.3m / WiFeS	600	3500-9550	NS
2012-Nov-18.42	+6.38	ANU-2.3m / WiFeS	600	3500-9550	NS
2012-Nov-19.56	+7.52	ANU-2.3m / WiFeS	900	3500-9550	MC
2012-Nov-20.30	+8.26	Lick-3m / Kast	360	3500-10300	SBC, OF
2012-Nov-20.48	+8.44	ANU-2.3m / WiFeS	900	3500-9550	MC
2012-Nov-21.24	+9.20	NTT-3.6m / EFOSC	100	3360-10000	PESSTO
2012-Nov-21.68	+9.64	ANU-2.3m / WiFeS	900	3500-9550	MC
2012-Nov-23.25	+11.21	NTT-3.6m / EFOSC	100	3360-10000	PESSTO
2012-Nov-29.42	+17.38	ANU-2.3m / WiFeS	900	3500-9550	CL, BS
2012-Dec-04.21	+22.17	NTT-3.6m / EFOSC	300	3360-10000	PESSTO
2012-Dec-08.50	+26.46	ANU-2.3m / WiFeS	900	3500-9550	ITH
2012-Dec-12.22	+30.18	NTT-3.6m / EFOSC	600	3360-10000	PESSTO
2012-Dec-17.41	+35.37	ANU-2.3m / WiFeS	900	3500-9550	JM, CD, SO
2012-Dec-21.22	+39.18	NTT-3.6m / EFOSC	900	3360-10000	PESSTO

^a With respect to B-band maximum at UT 2012-Nov-12.04

^b BK = Beth Klein, BS = Brad Schaefer, BZ = Ben Zuckerman, CD = Catherine de Burgh-Day, CL = Chris Lidman, CM1 = Curtis McCully, CM2 = Carl Melis, DB = Daniel Bayliss, DC = Dan Carson, EG = Elinor Gates, FV = Frédéric Vogt, GZ = George Zhou, ITH = I-Ting Ho, JF = Jerome Fang, JM = Jeremy Mould, KC = Kelsey Clubb, LP = Liuyi Pei, MB = Mike Bessell, MC = Mike Childress, MJ = Michael Jura, MO = Matt Owers. MP = Michael Pracy, NS = Nicholas Scott, NSL = Nicola S. Loaring, OF = Ori Fox, PK = Pat Kelly, SBC = S. Brad Cenko, SJ = Saurabh Jha, SK = Stefan Keller, SO = Sinem Ozbilgen, SX = Siyi Xu, TD = Tyler Desjardins

^c WiFeS red channel cryo pump failure

Table 2
SOFI Observation Details

UT Date	Phase (days)	Exposure Time (s)
2012-Nov-06.26	-5.78	480 (B) / 500 (R)
2012-Nov-14.35	+2.31	480 (B) / 500 (R)
2012-Nov-22.27	+10.23	480 (B) / 500 (R)
2012-Dec-05.27	+23.23	480 (B) / 500 (R)
2012-Dec-22.18	+40.11	480 (B) / 500 (R)

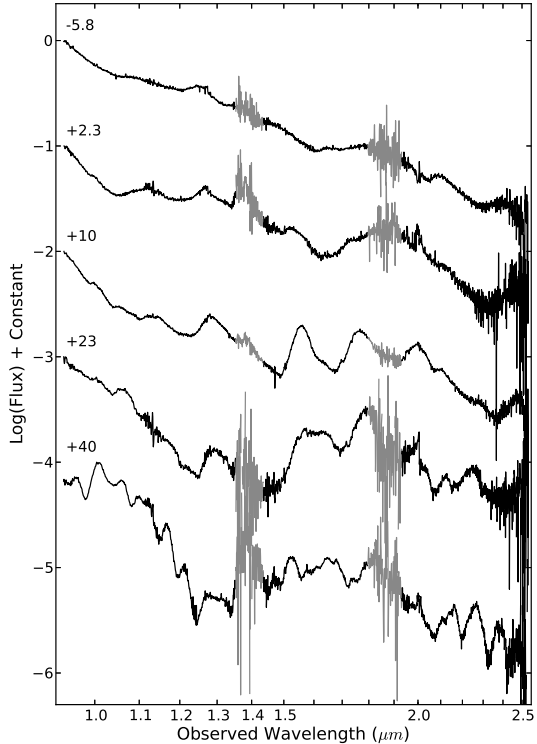


Figure 2. SN 2012fr SOFI spectra from PESSTO. Regions with strong telluric contamination have been plotted in grey.

for perhaps SN 2005hj whose similarly narrow line width was highlighted by Quimby et al. (2007). One can even visibly identify a flattening at the base of this feature due to the doublet nature of the line. We measure the observed linewidth (FWHM) to be $\sim 3400 \text{ km s}^{-1}$, and if we account for the 14\AA separation of the doublet lines would imply an intrinsic linewidth of $\sim 3000 \text{ km s}^{-1}$.

3.1. High-Velocity Si II $\lambda 6355$ in Early Spectra

At two weeks before maximum light, the Si II $\lambda 6355$ appears to be composed of a single broad, high-velocity component, but beginning around -12 days a second distinct component at lower velocities begins to develop. By -9 days the high velocity feature (HVF) and the lower velocity component exhibit equal strength, then by -5 days the HVF becomes difficult to distinguish visually.

While such Si II $\lambda 6355$ HVFs have been observed in

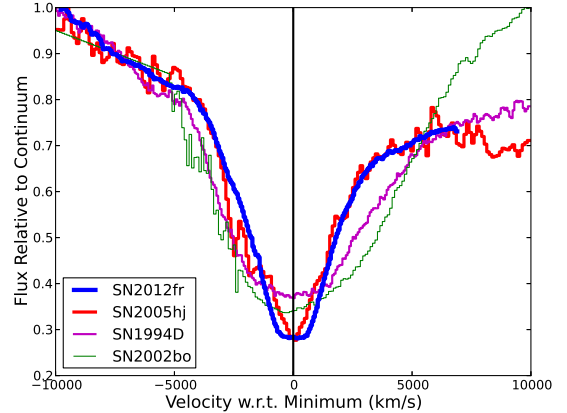


Figure 3. Si II $\lambda 6355$ feature for SN 2012fr (thick blue line) at +8 days in velocity space centered at the velocity minimum. Plotted for comparison are SN 2005hj (Quimby et al. 2007) at +9 days in red, SN 1994D at +11 days (from Blondin et al. 2012) in magenta, and SN 2002bo (Benetti et al. 2004) at +5 days in green, in order of thickest to thinnest lines.

other SNe Ia – notably SN 2005cf (Wang et al. 2009b) and SN 2009ig (Foley et al. 2012; Marion 2013), see also Section 6.1 – the distinction between HVF and photospheric components is cleaner in SN 2012fr than ever seen before. In this section we follow the evolution of the two components in a quantitative way by fitting the Si II $\lambda 6355$ line as a simple double-Gaussian profile.

We show in Figure 4 some example fits of the Si II $\lambda 6355$ line at several epochs. We first begin by defining regions of the blue and red pseudo-continuum, then perform a simple linear fit between the two regions. The flux in the line region is then divided by the pseudo-continuum and the normalized absorption profile is fitted with two Gaussians. The fit parameters are the center, width, and depth of each component, and the only constraints imposed are that the HVF component be above $14,000 \text{ km s}^{-1}$, and the low-velocity photospheric component be below that same threshold.

In Table 3 we present the fitted parameters for our two-component Si II $\lambda 6355$ fits including velocity center (v), velocity width (Δv , i.e. FWHM), and calculated pseudo equivalent width (pEW). In Figure 5 we show the velocity evolution of the two components compared to the v_{Si} evolution of other SNe Ia from Benetti et al. (2005). The HVF component shows a strong velocity gradient ($\dot{v}_{Si} = 353 \text{ km s}^{-1} \text{ day}^{-1}$) but at velocities much higher than that seen in normal SNe Ia, even at early times. The photospheric component, on the other hand, remains virtually constant in velocity even to late times (see Section 3.2) except for tentative evidence for higher velocity at the earliest epochs. However we caution that the photospheric component is much weaker than the HVF component at those phases so the velocity is more uncertain.

The relative strength of the two components is most clearly captured by examining the absorption strength of each component as quantified by the pseudo equivalent width (pEW). This can be trivially calculated as the area of the normalized absorption profile. We show in Figure 6 the pEW of the two fitted components from the earliest

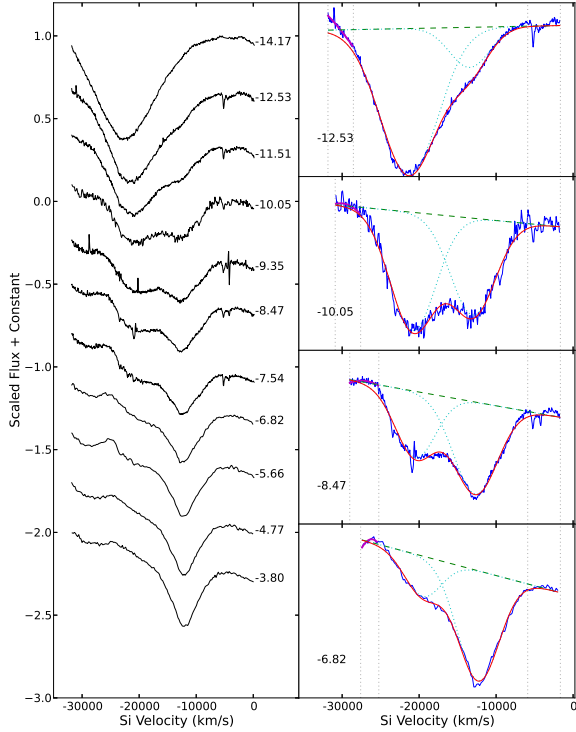


Figure 4. Left: Evolution of the Si II $\lambda 6355$ line for SN 2012fr in velocity space. Right: Several representative examples of the two-component Gaussian fits. Data are in blue, regions of the pseudo continuum fit are denoted by the vertical dotted black lines, the fitted pseudo continuum is the dashed green line, the fully fitted profile is shown as the smooth red line, and the two individual components are shown as the dotted cyan curves.

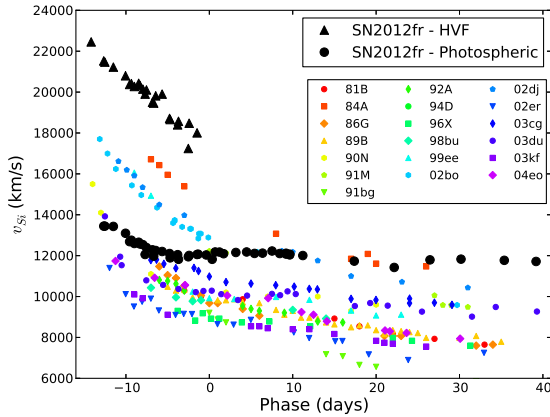


Figure 5. Velocity evolution of the Si II $\lambda 6355$ feature for SN 2012fr compared to a number of SNe Ia from the Benetti et al. (2005) sample. The HVF component for SN 2012fr is shown as the large black triangles, while the lower velocity photospheric component is shown as large black circles.

Table 3
Si II $\lambda 6355$ Fit Results

Phase (days)	Detached			Photospheric		
	v (km/s)	Δv (km/s)	pEW (\AA)	v (km/s)	Δv (km/s)	pEW (\AA)
-14.51	22704	11829	164.2	—	—	—
-14.17	22233	11587	171.6	—	—	—
-12.66	21525	9046	125.4	13444	6589	24.3
-12.53	21468	8898	120.2	13444	6294	23.0
-11.51	21223	7665	82.0	13430	6473	30.5
-10.05	20798	6315	43.5	13095	6547	38.0
-9.56	20374	6642	41.8	12685	6262	40.4
-9.35	20416	6326	37.6	12755	6431	43.0
-8.99	20275	6188	33.8	12595	6241	41.0
-8.47	20431	5767	29.5	12656	6347	46.8
-8.32	20327	5735	28.2	12571	6241	46.9
-7.97	20147	5503	22.6	12538	6041	46.2
-7.70	19902	6304	26.2	12057	6072	48.7
-7.54	20105	5735	24.5	12397	6167	51.3
-6.82	19501	5334	16.2	12284	5999	52.1
-6.67	19463	5545	16.2	11977	5978	53.6
-6.43	19817	4892	15.9	12251	6231	58.5
-5.66	19902	5651	16.1	12203	5841	55.5
-4.77	18713	5071	10.0	12104	5535	56.9
-4.70	18657	5345	9.8	11892	5619	58.3
-3.80	18397	5197	8.8	12048	5450	59.6
-3.70	18572	4892	5.5	11821	5398	58.4
-2.52	17242	4934	7.4	11944	5250	61.5
-2.42	18478	5693	8.0	12010	5377	63.9
-1.47	18006	4322	4.2	12057	5155	63.9
-0.37	—	—	—	12034	4965	63.4
+0.34	—	—	—	11821	4776	61.7
+0.70	—	—	—	12180	4755	62.9
+1.22	—	—	—	12175	4818	64.0
+1.71	—	—	—	12095	4617	62.8
+3.18	—	—	—	12156	4533	64.0
+4.47	—	—	—	12180	4270	62.3
+5.42	—	—	—	12109	4185	62.2
+6.38	—	—	—	12123	4132	62.4
+7.52	—	—	—	12227	3995	61.4
+8.44	—	—	—	12104	3953	61.1
+9.20	—	—	—	12118	3953	60.7
+9.64	—	—	—	12071	3953	61.3
+11.21	—	—	—	12006	—	—
+17.38	—	—	—	11732	—	—
+22.17	—	—	—	11423	—	—
+26.46	—	—	—	11794	—	—
+30.18	—	—	—	11829	—	—
+35.37	—	—	—	11771	—	—
+39.18	—	—	—	11716	—	—

epoch (-13 days) to the latest epoch (-1 days) at which both features have a significant detection, and for the full Si II $\lambda 6355$ profile for all epochs before +10 days. As previously noted, the strength of the HVF fades very quickly while that of the photospheric component slowly rises, with the equality point occurring between -10 and -9 days. The total pEW of the Si II $\lambda 6355$ line declines until a few days before maximum light when it remains nearly constant at around 65 \AA . As we will discuss below (Section 5), the pEW of this line is lower in SN 2012fr than in many other normal SNe Ia as measured in the BSNIP sample (Silverman et al. 2012b,a).

3.2. Full Velocity Evolution of Si II $\lambda 6355$

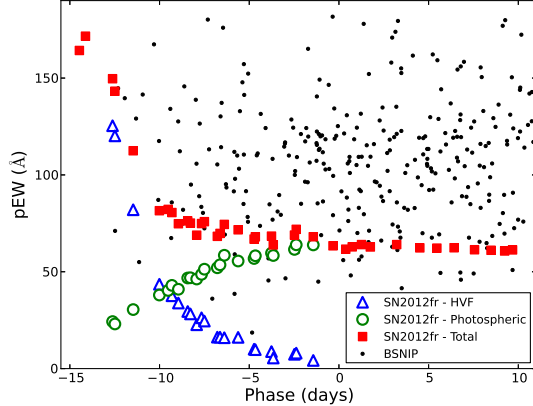


Figure 6. Pseudo equivalent width (pEW) of the Si II $\lambda 6355$ components for SN 2012fr as a function of phase. When both HVF and photospheric component are clearly detected, they are shown as open blue triangles and open green circles, respectively. Total pEW of the Si II $\lambda 6355$ line is shown as filled red squares. For references, the BSNIP sample (Silverman et al. 2012b,a) is shown as small black points.

After the HVF Si II $\lambda 6355$ feature fades, the main photospheric component is well fit by a single Gaussian until about two weeks after maximum light. At that time, Fe lines to the red and blue of the Si II $\lambda 6355$ begin to develop significant opacity and make it impossible to correctly determine the pseudo-continuum of the Si II $\lambda 6355$ line.

Thus for the epochs +17 days and later, we fit the velocity minimum of the Si II $\lambda 6355$ by fitting a simple Gaussian profile only in a region of width 30 \AA centered on the Si II $\lambda 6355$ minimum. Remarkably, the velocity of the line minimum remains nearly constant at about $11,800 \text{ km s}^{-1}$ even out to phase +39. This is confirmed by visual inspection of the Si II $\lambda 6355$ region as plotted in Figure 7. We do note that at such late epochs, emission becomes increasingly important (see e.g. van Rossum 2012) in the line profiles, so it is possible that the flux minimum may not necessarily trace the true $\tau = 1$ surface.

We see once again that the narrow width of the photospheric lines provides an advantage in following the Si II $\lambda 6355$ velocity reliably to very late epochs. The Fe lines to the red and blue of this feature are clearly distinguished in SN 2012fr, enabling an accurate isolation of Si II $\lambda 6355$ and a reliable measurement of its velocity. In most other SNe Ia, the broader line widths result in a blend of the Si II $\lambda 6355$ with its neighboring Fe lines, making velocity measurements difficult at late epochs. We will return to this point in Section 6.1.

4. ADDITIONAL ATOMIC SPECIES IN SN 2012FR SPECTRA

The narrow velocity width of the photospheric Si II $\lambda 6355$ line noted in Section 3 holds true for nearly all absorption features in the optical spectra of SN 2012fr starting about a week after maximum light. This provides a unique advantage in line identifications in the SN spectra, as blending of neighboring lines is less pronounced in SN 2012fr than in many other SNe Ia.

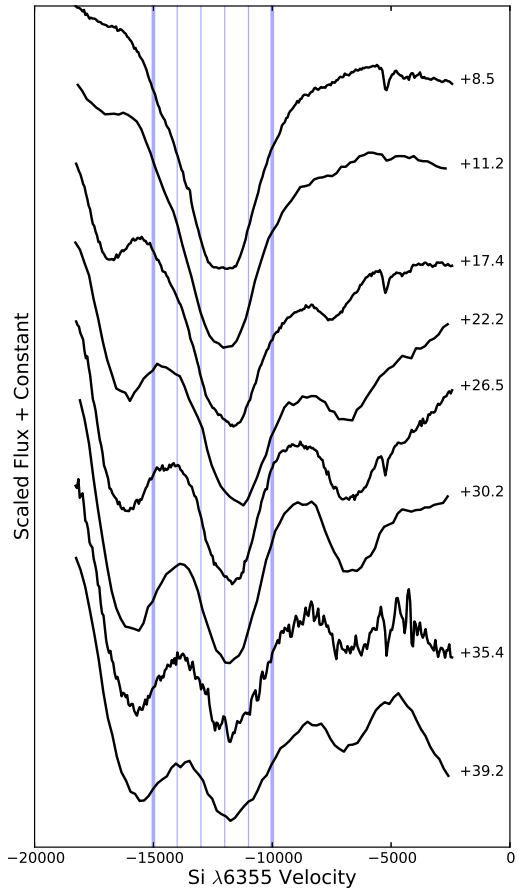


Figure 7. Late time evolution of the Si II $\lambda 6355$ line in SN 2012fr, shown in velocity space. The wavelengths corresponding with $10,000 \text{ km s}^{-1}$ and $15,000 \text{ km s}^{-1}$ are shown as thick blue lines, with $1,000 \text{ km s}^{-1}$ intervals between denoted by thin blue lines. The velocity plateau at late times appears around $11,800\text{--}12,000 \text{ km s}^{-1}$.

In this Section we focus on four element groups of particular interest. We begin by inspecting narrow Na I D absorption in Section 4.1, and show that SN 2012fr shows no detectable reddening by dust. In Section 4.2 we briefly present our search for signatures of unburned carbon in SN 2012fr, which showed no clear detection. In Section 4.3 we inspect the Ca II IR triplet, which exhibits similar behavior as the Si II $\lambda 6355$, then briefly examine the more complex Ca II H&K line at maximum light. Finally in Section 4.4, we examine the velocities of Fe group elements in SN 2012fr.

4.1. Na I D Narrow Absorption

Narrow absorption in the Na I D line in SN Ia spectra is commonly used to quantify the amount of foreground dust that reddens a SN Ia. Na I D absorption at the redshift of the SN host galaxy presumably arises from either foreground interstellar dust (e.g. Poznanski et al. 2011, 2012) or very nearby circum-

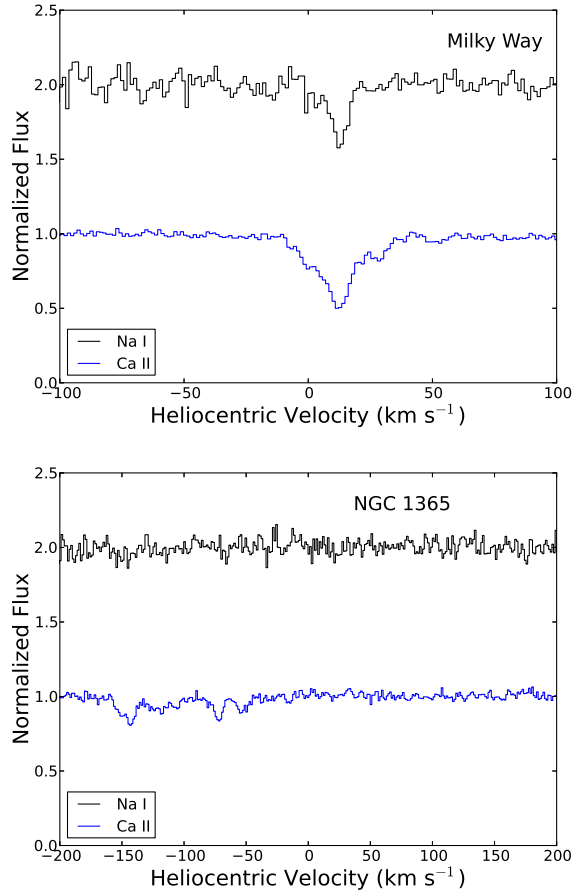


Figure 8. Keck HIRES observations of SN 2012fr. Top: Narrow Na I D and Ca II H&K at rest velocity, arising from Milky Way dust. Bottom: Narrow Na I D and Ca II H&K at the recession velocity of NGC 1365.

Table 4
HIRES absorption equivalent widths

Line	Milky Way (mÅ)	NGC 1365 (mÅ)
Ca II 3934.777	129.3 ± 3.6	107.3 ± 7.0
Ca II 3969.591	66.0 ± 4.0	57.3 ± 6.0
Na I 5891.5833	82.9 ± 13.8	< 42.0 (3σ)
Na I 5897.5581	35.4 ± 13.4	< 40.8 (3σ)

stellar material shed from the SN progenitor system prior to explosion (Patat et al. 2007; Simon et al. 2009; Sternberg et al. 2011; Dilday et al. 2012).

SN 2012fr shows no detectable narrow Na I D absorption in the HIRES spectrum taken at phase -13.6 days. In Figure 8 we show the regions of the HIRES spectrum corresponding to the Na I D line as well as the Ca II H&K lines, both at the redshift of the host galaxy NGC 1365 ($v = 1636 \text{ km s}^{-1}$ – Bureau et al. 1996) and at zero redshift. Measurements of the line detections, or 3σ upper limits, are presented in Table 4.

Narrow absorption features from Milky Way dust are clearly detected at 2.6σ and 6.0σ in the D1 and D2 lines of Na I, and at very high significance ($> 10\sigma$) in the H&K lines of Ca II. Using the empirical scaling relations

of Poznanski et al. (2012) to convert Na I D absorption into the reddening $E(B - V)$, the measured D1 and D2 absorption strengths imply reddening of $E(B - V) = 0.0186$ and $E(B - V) = 0.0213$, respectively. These are in excellent agreement with the measured value of $E(B - V) = 0.018$ from Schlafly & Finkbeiner (2011).

The only possible absorption features at the redshift of NGC 1365 appear in the Ca II H&K lines at about $v = -100 \text{ km s}^{-1}$ from the rest redshift of NGC 1365. Given that these features lack corresponding features in Na I D, in addition to the facts that NGC 1365 is a nearly face-on barred spiral and SN 2012fr is very close to the center of the galaxy, it appears unlikely that this feature near Ca II H&K is truly caused by interstellar dust. Thus, we detect no significant interstellar reddening for SN 2012fr. The strongest constraint arises from the D2 line of Na I D which places a 3σ upper limit of $E(B - V) < 0.015$ (again using Poznanski et al. 2012) for the reddening of SN 2012fr from within NGC 1365.

4.2. C II

We comment briefly in this section on the search for unburned carbon features in the spectra of SN 2012fr. Such signatures typically manifest as weak C II absorption lines in optical spectra of SNe Ia, and have been of particular interest in recent years (Thomas et al. 2011b; Parrent et al. 2011; Folatelli et al. 2012; Silverman & Filippenko 2012; Blondin et al. 2012). The strongest carbon feature in the optical is typically the C II $\lambda 6580$ line, and the slightly weaker $\lambda 7234$, $\lambda 4745$, and $\lambda 4267$ lines of C II are also sometimes visible (e.g. Mazzali 2001; Thomas et al. 2007).

The redshift of NGC 1365 places the likely location of the strongest C II feature ($\lambda = 6580$) coincident with a weak telluric absorption feature at $\lambda = 6280$ (corresponding to $v \sim 13,700 \text{ km s}^{-1}$ for C II $\lambda 6580$). Though this telluric feature is weak, it is of comparable strength to the typical C II absorption. We cannot identify any obvious signature of C II $\lambda 6580$ absorption on top of this telluric feature, nor do we detect the other major C II lines in the optical even at early epochs.

This is demonstrated directly in Figure 9, where we plot the four C II line regions in velocity space for the -14.17 day spectrum from SALT. No clear signature of C II seems visible in any of these lines, even for C II $\lambda = 6580$ after correction of the telluric feature. C I features in the NIR may provide better detection of unburned material in SN 2012fr (see e.g. SN 2011fe in Hsiao et al. 2013), and will be investigated with detailed spectroscopic fitting in Paper III (Hsiao et al., 2013, in prep.).

4.3. Ca II

4.3.1. Ca II IR triplet

The Ca II IR triplet in SN 2012fr begins at very high velocities two weeks before maximum light, with the blue edge of the absorption in the first spectrum reaching relativistic velocities of nearly $50,000 \text{ km s}^{-1}$ ($v \sim 0.17c$). The line complex gradually recedes in velocity and exhibits complex structure roughly a week before maximum light, then by two weeks after max appears dominated by a single narrow component.

The complex structure of the Ca II IR triplet appears

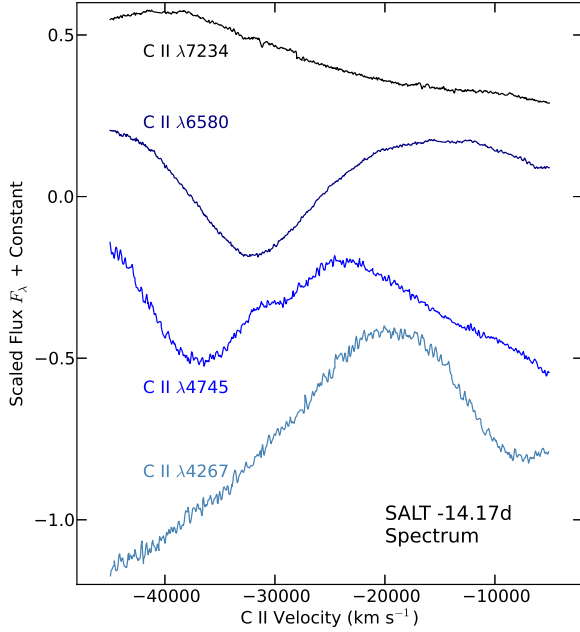


Figure 9. Regions of the -14.17 day SALT spectrum of SN 2012fr corresponding to the strongest typical C II features in SNe Ia, plotted in terms of velocity of the respective lines.

to be indicative of multiple components in velocity space, similar to that seen in the Si II $\lambda 6355$ (see Section 3.1). Modeling this line multiplet is more complex than the simple two-component Gaussian fits employed for the Si II $\lambda 6355$. Instead, each component of the Ca II IR triplet in velocity space must be modeled as a triplet of Gaussian profiles with common velocity width, separation in velocity space as dictated by the line rest wavelengths, with relative absorption depths constrained by atomic physics (i.e. their relative B values, though see discussion below about optical depth effects).

For epochs where spectral wavelength coverage extended red enough to cover the Ca II IR triplet, we fit the absorption profile as a two component model after normalizing to a fitted pseudo-continuum. Each absorption component is described by a central velocity, velocity width and absorption depth (here we set relative absorption depths of the triplet lines by their B values, i.e. assuming the optically thin regime). As with the Si II $\lambda 6355$, the only constraint applied here was to force the two components to occupy different regions of velocity space split at $14,000 \text{ km s}^{-1}$. We show the spectral evolution of the Ca II IR triplet as well as some representative profile fits in Figure 10. As with the Si II $\lambda 6355$ fits, the pseudo-continuum shape begins to be poorly represented by a simple linear fit at late times. Thus we employ a similar Gaussian line minimum fitting technique as that employed for the Si II $\lambda 6355$ for epochs after +12 days, here measuring the minimum of the cleanly separated 8662 \AA line.

We report results in Table 5, with fit parameters labeled similarly as in Table 3. The high velocity component consistently exhibits a broad velocity width ($> 5000 \text{ km s}^{-1}$) producing a broad component where all

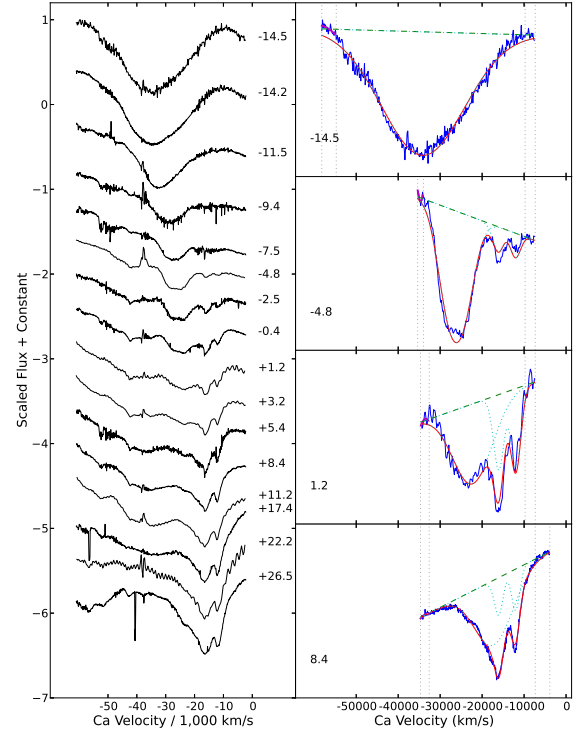


Figure 10. Same as Figure 4 but for the Ca II IR triplet. Here velocities are plotted with respect to the reddest line in the Ca II IR triplet at 8662 \AA .

lines in the triplet are blended. The low velocity component exhibits the same narrow velocity width as observed in the Si II $\lambda 6355$ line, making it possible to distinguish the 8662 \AA line from the 8542 \AA line (which is blended with the much weaker 8498 \AA line). This is illustrated directly in Figure 11, where we show the Ca II IR triplet evolution at late times and demonstrate the ability to both resolve the triplet lines and observe their consistent velocity at $v \sim 12,000 \text{ km s}^{-1}$.

In Figure 12 we plot the velocity evolution of the fitted Ca II IR triplet components compared to the analogous components in the Si II $\lambda 6355$ line (Section 3). The HVF Ca II IR triplet component is consistently at higher velocities than the Si II $\lambda 6355$ HVF, has a steeper velocity gradient ($\dot{v}_{Ca} = 686 \text{ km s}^{-1} \text{ day}^{-1}$), and is visible to later epochs than the Si II $\lambda 6355$ HVF (we note these characteristics were also notably observed in the Ca II IR triplet feature for SN 2009ig – Marion 2013). In SN 2012fr the late-time velocity of the Ca II IR triplet plateaus at about $v \sim 12,000 \text{ km s}^{-1}$, consistent with the velocity plateau observed in the Si II $\lambda 6355$ line.

Finally we note that the results presented above use Ca II IR triplet model profiles which assume the optically thin regime. In this limit the ratios of the line absorption strengths (specifically, the equivalent widths) in the triplet are directly proportional to the Einstein B values, whereas in the optically thick regime the ratios of the line equivalent widths would approach unity. We repeated the above fits under the optically thick assump-

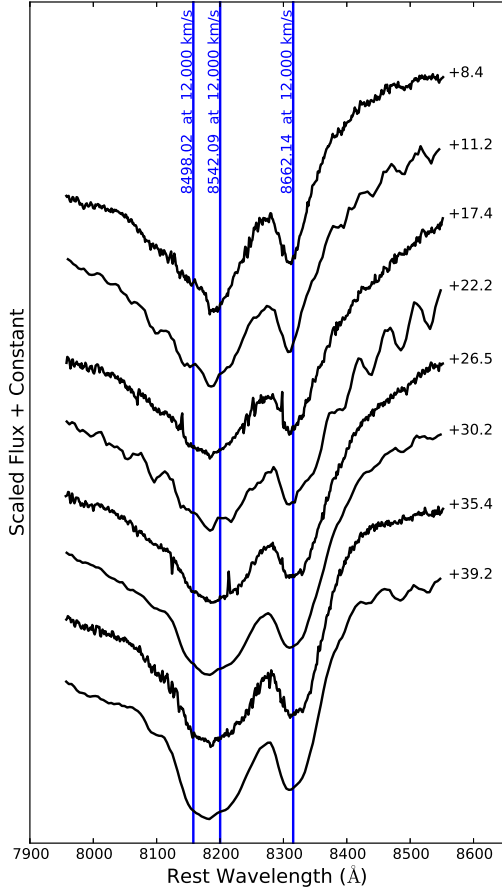


Figure 11. Late epoch evolution of the Ca II IR triplet for SN 2012fr, showing the narrow velocity width and constant velocity of the three lines comprising the triplet. For reference, we mark the wavelengths of the three triplet lines at a velocity of $v = 12,000 \text{ km s}^{-1}$, showing that the reddest line of the triplet at 8662\AA is cleanly resolved from the bluer two lines.

tion and found that while the fits were slightly worse, the qualitative behavior of the velocity evolution was consistent with that found in our fiducial fits. The velocities on average were lower than the fiducial fitted values due to the shift in weighted mean wavelength of the triplet, but the late time velocity was still consistent with the $v \sim 12,000 \text{ km s}^{-1}$ velocity plateau due to the 8662\AA line being distinguishable from the bluer lines in the triplet. The true absorption strengths of the lines in the Ca II IR triplet likely fall somewhere between the optically thin and optically thick regimes, but we have confirmed that our results are consistent in both extreme cases.

4.3.2. Ca II H&K

The Ca II H&K doublet is a line complex of keen interest for SNe Ia, as its behavior at maximum light may be an indicator of intrinsic SN Ia color (Foley et al. 2011; Chotard et al. 2011; Blondin et al. 2012; Foley 2012). Additionally, recent work by Maguire et al.

Table 5
Ca II IR triplet Fit Results

Phase (days)	Detached			Photospheric		
	v (km/s)	Δv (km/s)	pEW (Å)	v (km/s)	Δv (km/s)	pEW (Å)
-14.51	32093	21838	611.6	—	—	—
-11.51	29657	15403	364.7	—	—	—
-9.35	26817	8899	135.4	—	—	—
-7.54	25572	4514	85.6	—	—	—
-4.77	24208	5739	97.5	12091	2726	14.0
-2.52	23076	6747	96.5	11916	2699	29.6
-0.37	21688	8291	98.4	11928	2782	43.1
+1.22	20335	9138	97.7	11966	2670	47.6
+3.18	18677	9771	105.8	11986	2570	49.9
+5.42	17089	9024	119.6	12016	2538	51.0
+8.44	15404	8723	143.0	12014	2170	37.2
+11.21	14303	8537	173.0	12092	1676	20.8
+17.38	—	—	—	12092	—	—
+22.17	—	—	—	12121	—	—
+26.46	—	—	—	11976	—	—
+30.18	—	—	—	12082	—	—
+35.37	—	—	—	11937	—	—
+39.18	—	—	—	12052	—	—

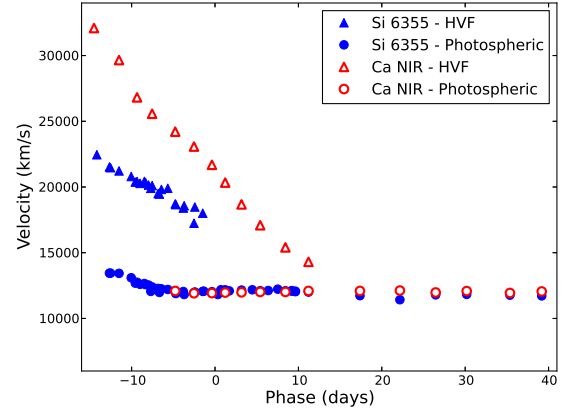


Figure 12. Velocity evolution of the high-velocity (triangles) and photospheric (circles) components of the Ca II IR triplet (open red symbols) in SN 2012fr compared to that of the Si II $\lambda 6355$ line (filled blue symbols).

(2012) showed that the Ca II H&K velocity of the mean fast-declining (low “stretch”) SN Ia spectrum at maximum light is lower than that for the mean slow-declining (high “stretch”) SN Ia spectrum. Thus, the Ca II H&K line seems a promising source for unraveling SN Ia diversity.

Interpreting Ca II velocities with this line complex is difficult, however, due to the presence of the nearby Si II $\lambda 3858$ line (see thorough discussion in Foley 2012), as well as the complex underlying pseudo-continuum. We therefore chose to examine this line complex only at maximum light for SN 2012fr. We employed a fitting procedure similar to that of the Ca II IR triplet but with fit parameters informed and tightly constrained by results of the Ca II IR triplet and Si II $\lambda 6355$ fits. In Figure 13 we show the result of our line profile fit where we model absorption in Ca II H&K line with multiple velocity com-

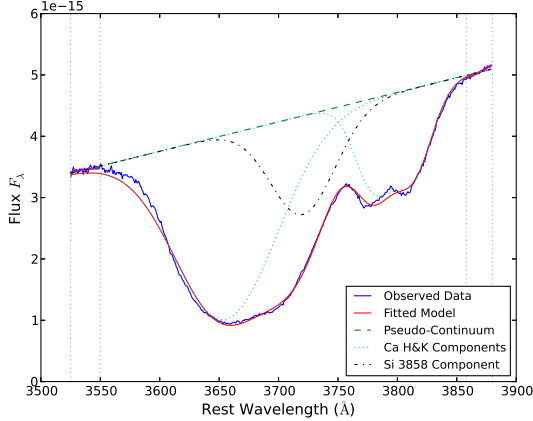


Figure 13. Fit to the Ca II H&K line profile in the maximum light (WiFeS Nov 11.67) spectrum of SN 2012fr. Line colors and styles are the same as in Figure 4, but with the Si II $\lambda 3858$ line profile plotted as the dashed-dotted black line.

ponents, where each velocity component is a doublet profile with relative depths set by the B values (whose ratio is already close to 1, making the observed absorption ratio effectively insensitive to optical depth). In addition to the HVF and photospheric components of the Ca II H&K line, we add a single Gaussian absorption profile to model Si II $\lambda 3858$.

We constrained the velocity center and velocity widths of the two Ca II H&K components to be within 20% of their values fitted for Ca II IR triplet, but left the absorption depths as free parameters. Similarly, we forced the velocity width and center of the Si II $\lambda 3858$ line to be within 20% of the Si II $\lambda 6355$ line. The nominal fit results showed velocity centers for the three components to be very close ($< 1000 \text{ km/s}$ difference) to the values from their red counterparts. The Si II $\lambda 3858$ line, low-velocity Ca II H&K, and high-velocity Ca II H&K components had absorption pEW values of 25.2\AA , 23.5\AA , and 79.4\AA . Thus our fits indicate that both Ca II H&K and Si II $\lambda 3858$ are needed to explain the absorption profile, with the HV Ca II H&K being dominant over the Si II $\lambda 3858$.

We note however that the quantitative details of these results are dependent on how tightly we constrain the velocity width of the HV Ca II H&K component. If we loosened the constraints to be within 30% of the Ca II IR triplet velocity width, it changes the pEW of the HV Ca II H&K and Si II $\lambda 3858$ lines to be 68\AA and 35\AA , respectively. This is because the high velocities of the HV Ca II H&K component place it nearly coincident with the wavelength of the lower velocity Si II $\lambda 3858$ line. We therefore cannot say conclusively what the absorption ratio of these two lines is in this line complex, but we did find consistently that both were needed to adequately fit the absorption profile.

We found here that decoupling the Si II $\lambda 3858$ line from the Ca II H&K line is a nontrivial procedure. While it is difficult to derive precise quantitative results, two general qualitative results are clear. The first is that both the Ca II H&K line and the Si II $\lambda 3858$ line are operative in this line complex for SN 2012fr, and that high velocity

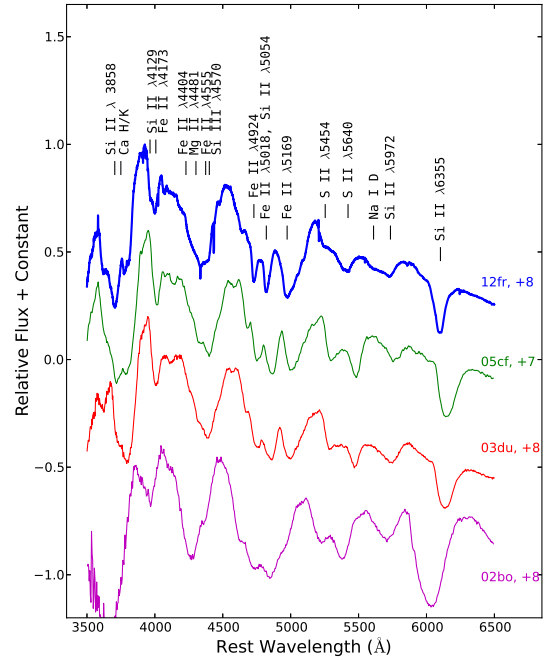


Figure 14. Line identifications for SN 2012fr (blue) for the +8 day spectrum, compared to the spectra of other SNe Ia at a similar epoch. SN 2005cf (Wang et al. 2009b), SN 2003du (Stanishev et al. 2007), and SN 2002bo (Benetti et al. 2004) are shown as the green, red, and magenta spectra, respectively.

Ca II H&K can be nearly degenerate with lower velocity Si II $\lambda 3858$. The second conclusion for SN 2012fr is that regardless of the details of how much the line velocities and velocity widths are allowed to vary, high-velocity Ca II H&K appears to be the dominant contributor to absorption in this line region.

4.4. Fe Group Elements

The narrow line widths of SN 2012fr are useful for identifying absorption features which are typically blended in other SNe Ia, and are particularly advantageous for identifying Fe lines. In Figure 14 we illustrate this principle with the +8 days spectrum of SN 2012fr compared to two other “normal” SNe Ia, SN 2005cf (Wang et al. 2009b) and SN 2003du (Stanishev et al. 2007), as well as the broad-lined SN 2002bo (Benetti et al. 2004). Of particular note is the line complex at around 4700\AA comprising several Fe II lines and the Si II $\lambda 5054$ line which shows cleaner separation in SN 2012fr than the other SNe Ia.

In the +8 day spectrum, three major Fe II lines ($\lambda 4924$, $\lambda 5018$, and $\lambda 5169$) all have velocity minima consistent with the velocity plateau ($v \sim 12,000 \text{ km s}^{-1}$) identified in Si II $\lambda 6355$. We illustrate this in Figure 15 where we plot the post-maximum spectra of SN 2012fr in the relevant wavelength region and highlight the wavelengths associated with each of these lines at $v = 12,000 \text{ km s}^{-1}$. After this epoch, the observed velocity minima of these Fe lines decrease with time. We also tentatively identify two features which may be associated with Cr II lines ($\lambda 4876$ and $\lambda 5310$), though their velocity evolution is

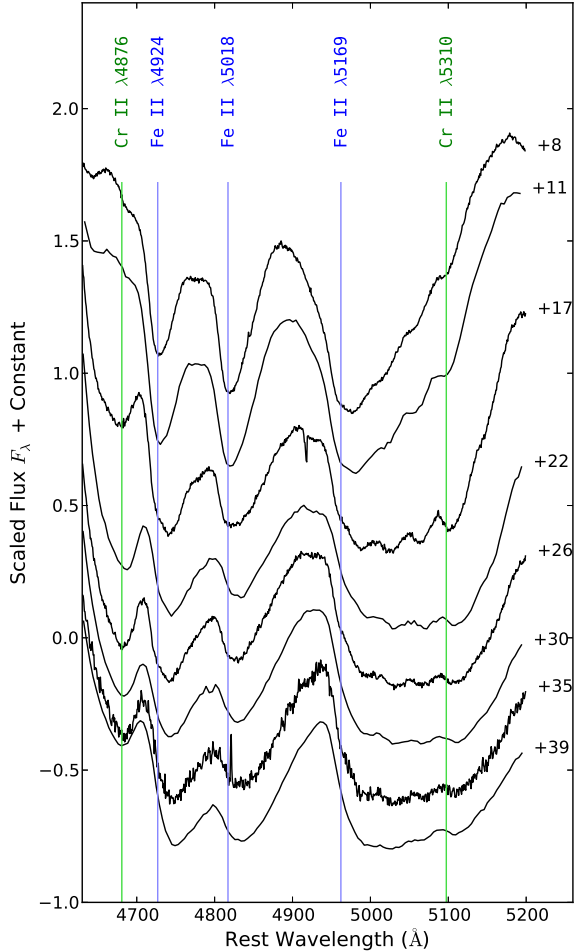


Figure 15. Post-maximum spectra of SN 2012fr highlighting selected region with significant Fe group element features. Vertical lines correspond to wavelength of labeled features at a velocity of $v = 12,000 \text{ km s}^{-1}$, the velocity measured for Fe II features in the +8 days spectrum.

more difficult to follow due to the strongly evolving shape of the underlying pseudo-continuum. We note here that these lines which we attribute to Fe group elements show no clear signature of high velocity features in the early spectra of SN 2012fr (some Fe H VFs have been possibly identified in several SNe Ia, e.g. Branch et al. 2004; Mazzali et al. 2005a; Marion 2013), though further modeling of the spectra may reveal subtler insights.

The velocity behavior of the Fe group lines indicates that the $\tau = 1$ surface of the photosphere is at $v \sim 12,000 \text{ km s}^{-1}$ at one week after maximum, then recedes inward after that time. From this we can conclude two important results: (i) the Si and Ca velocity plateaus imply that the layer of IMEs is unlikely to extend deeper than $v \sim 12,000 \text{ km s}^{-1}$ since the Fe group elements are detected at lower velocities on the same epochs; and (ii) the layer of Fe group elements extends deeper in the ejecta than the IMEs, indicating a likely stratification of the ejecta.

While these preliminary line identifications are interesting, a full accounting of all elements and their

Table 6
Spectral Indicators for SN 2012fr

Quantity	Value	Unit
$\Delta m_{15}(B)$	0.80 ± 0.01	mag
$pEW(5972)$	3.9 ± 5.0	Å
$pEW(6355)$	66.5 ± 15.5	Å
$v_{Si} \text{ (max)}$	12037 ± 200	$\text{km} \cdot \text{s}^{-1}$
\dot{v}_{Si}	0.3 ± 10.0	$\text{km} \cdot \text{s}^{-1} \cdot \text{day}^{-1}$

velocities would require a spectrum synthesis fit (see e.g. Thomas et al. 2011a) such as that undertaken by Parrent et al. (2012) for SN 2011fe (Nugent et al. 2011), or a modeling of abundance stratification in the ejecta such as that undertaken by Stehle et al. (2005). Such analyses are beyond the intended scope of this paper, but we believe that the spectra released here will be invaluable for such efforts and we strongly encourage future modeling of the SN 2012fr spectra.

5. SPECTROSCOPIC SUB-CLASSIFICATION OF SN 2012FR

In recent years much effort has been focused on categorizing the observed diversity of SNe Ia by means of quantitative metrics measured from their optical spectra. In this section we will examine SN 2012fr in the context of these classification schemes. The spectral indicator values for SN 2012fr employed for that purpose are presented in Table 6. These include several quantities ($pEW(5972)$, $pEW(6355)$, v_{Si}) calculated from the maximum light spectrum (the Nov. 11.67 WiFeS spectrum), the velocity gradient of the Si II $\lambda 6355$ line \dot{v}_{Si} (measured from the absolute decline between phases 0 and +10), and the light curve decline rate $\Delta m_{15}(B)$ (from Paper I). We note that the pEW values used here are calculated from direct integration of the line profile and differ insignificantly from the Gaussian area reported in Section 3.1.

Branch et al. (2009) proposed that SNe Ia be split into four broad categories based on their location in the parameter space defined by the pseudo equivalent width (pEW) of Si II $\lambda 5972$ and $\lambda 6355$ lines. We show SN 2012fr on this “Branch diagram” in the upper left panel of Figure 16, along with a sample of SNe Ia combining the samples of Blondin et al. (2012) and Silverman et al. (2012a). SN 2012fr falls on the boundary between the “shallow silicon” class and the “core normal” class. As previously noted by both Silverman et al. (2012a) and Blondin et al. (2012), these Branch classes do not represent disjoint samples with distinct features but instead represent regions within a continuum of SN Ia characteristics. SN 2012fr appears to be a clear example of a transition-like event that bridges the gap between two sub-classes.

Wang et al. (2009a) showed that a subset of SNe Ia display high velocities in the Si II $\lambda 6355$ line, and this “HV” subset exhibits different color behavior than SNe Ia with normal velocities. In the upper right panel of Figure 16 we show SN 2012fr on the “Wang diagram” which plots $pEW(6355)$ vs. v_{Si} at maximum light, as well as the same comparison sample of SNe Ia from the Branch diagram. Once again, SN 2012fr has a v_{Si} value which is just slightly above the established boundary separating HV

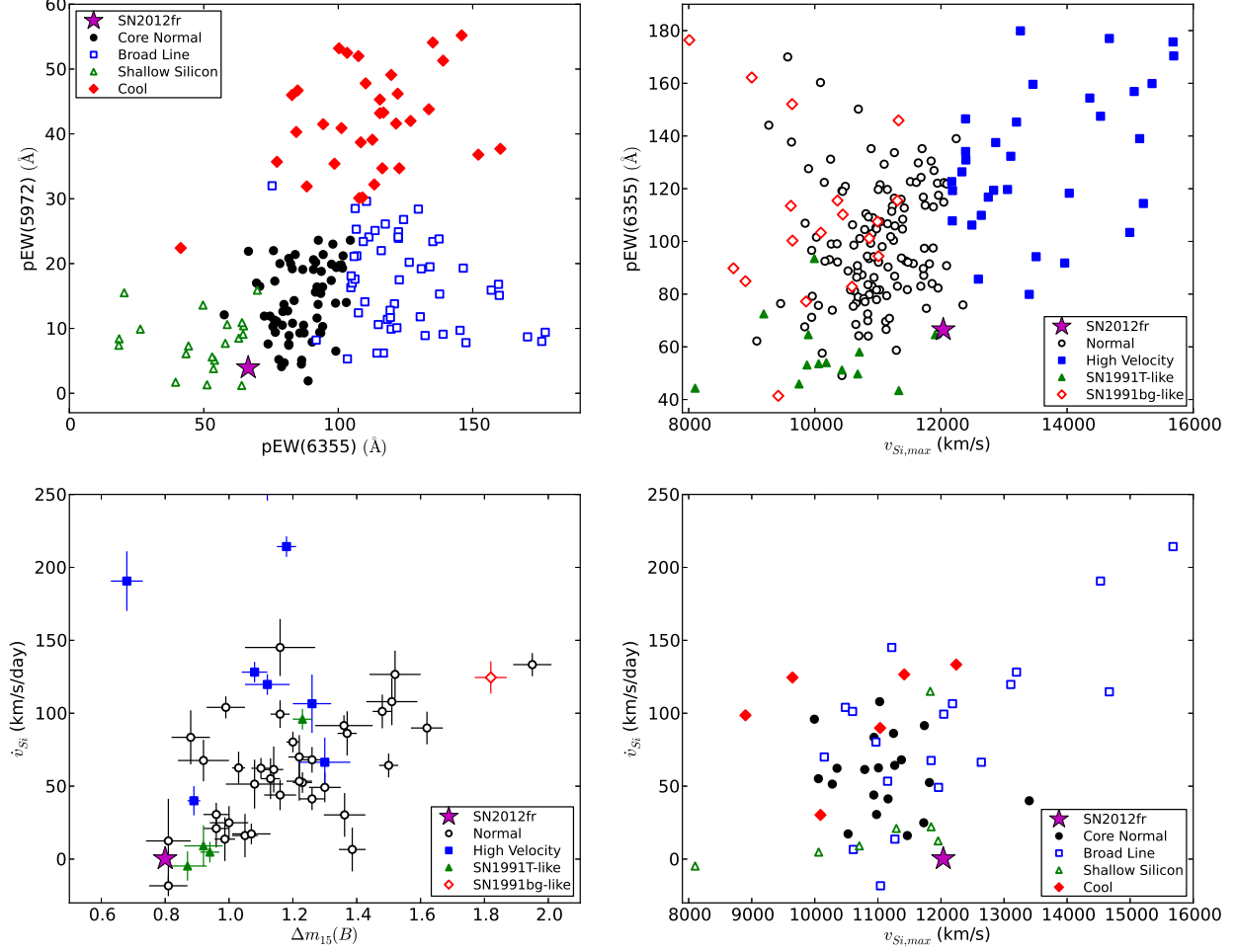


Figure 16. Spectral indicators from SN 2012fr compared to other SNe Ia as measured in Blondin et al. (2012) and Silverman et al. (2012a). Top Left: $pEW(5972)$ vs. $pEW(6355)$ at maximum light with spectroscopic sub-classes defined as in Branch et al. (2009). Top Right: $pEW(6355)$ vs. v_{Si} at maximum light with velocity-based sub-classes as defined in Wang et al. (2009a). Bottom Left: Velocity gradient of the Si II $\lambda 6355$ line \dot{v}_{Si} , as measured from the absolute decline between phases 0 and +10, vs. light curve decline rate $\Delta m_{15}(B)$, as previously inspected by Benetti et al. (2005). Bottom Right: Velocity gradient vs. v_{Si} at maximum light.

from normal SNe Ia, marking it as a transition-like event between velocity classes. Its location in this diagram is noteworthy because it exhibits a lower $pEW(6355)$ than any of the other HV SNe Ia, and its velocity is higher than other SNe Ia with weak Si II $\lambda 6355$ absorption.

Benetti et al. (2005) examined subclasses of SNe Ia based on the velocity evolution of the Si II $\lambda 6355$ line. They found that fast-declining SNe Ia tended to have consistently high velocity gradients (dubbed the “faint” sub-class), while slow-declining SNe Ia appeared to occur in two classes with either high or low velocity gradients (“HVG” and “LVG”, respectively). In the bottom left panel of Figure 16, we show SN 2012fr on this “Benetti diagram” along with the subset of SNe Ia from the other panels with sufficient data to measure a velocity gradient. SN 2012fr clearly resides in the LVG region of this diagram, as expected due to the observed Si II $\lambda 6355$ velocity plateau (see Section 3.2).

Finally, in the bottom right panel of Figure 16 we show the velocity gradient versus velocity at maximum light. As has been previously noted, the HV objects appear to show a correlation between their velocity gradient and velocity at maximum light. SN 2012fr has a lower veloc-

ity gradient than any of the HV members, and instead appears to reside at the edge of the cloud of points populated by normal velocity SNe Ia.

SN 2012fr exhibits much of the spectroscopic and photometric behavior of the more luminous SNe Ia such as SN 1991T (Phillips et al. 1992; Filippenko et al. 1992) or SN 1999aa (Garavini et al. 2004). It has a slow light curve decline rate, relatively shallow Si II absorption at maximum light, and a very low velocity gradient in the Si II $\lambda 6355$ line. However, two key features of SN 2012fr are not observed in 99aa-like or 91T-like SNe Ia: the high velocity of the Si II $\lambda 6355$ line (both at maximum light in the photospheric component and in the early HVF component), and strong absorption in the Si II $\lambda 6355$ line at early epochs (phase about -10 days).

In Figure 17 we compare the spectra of SN 2012fr at -12 days and at maximum light to comparable spectra from the 91T-like SN 1998es (from Blondin et al. 2012), SN 1999aa (from Blondin et al. 2012), and the normal SNe Ia SN 2005cf (Wang et al. 2009b) and SN 2003du (Stanishev et al. 2007). We see that at maximum light SN 2012fr shows slightly weaker Si II $\lambda 5972$ and Si II $\lambda 6355$ than the normal SNe Ia, but higher velocity and

stronger Ca H&K absorption than SN 1999aa and the 91T-like SN. At very early epochs (-12 days) SN 2012fr is very dissimilar to the extreme slow-decliners, as it displays stronger absorption in Si II $\lambda 6355$ and the “sulfur W”, and it lacks the characteristic strong Fe absorption found in 99aa/91T-like SNe Ia. The stronger absorption and higher velocities of the photospheric components of the Si II $\lambda 6355$ line and the lack of strong Fe absorption also argue against the possibility of SN 2012fr being a 99aa/91T-like SN Ia with HVFs superposed on its spectrum. Thus while SN 2012fr shares a number of characteristic with these extremely slow declining SNe Ia, it does not exhibit sufficient spectroscopic similarity to be classified as a member of those peculiar SN Ia sub-classes.

6. DISCUSSION

The spectra of SN 2012fr exhibited several noteworthy characteristics: (1) a very narrow velocity width in the photospheric absorption lines for phases later than one week after maximum light; (2) high velocity Si II $\lambda 6355$ and Ca II IR triplet features which could be cleanly decoupled from the lower velocity photospheric component; (3) a clear plateau in the Si II $\lambda 6355$ velocity, as well as the Ca II IR triplet velocity, extending out until +39 days; (4) silicon absorption line strengths placing it on the borderline between “shallow silicon” and “core normal” classes; and (5) silicon velocity placing it on the borderline between “normal” and “high velocity” SNe Ia.

In this section we first reflect on what the Si II $\lambda 6355$ velocity behavior of SN 2012fr can teach about interpretation of this velocity evolution in other SNe Ia (Section 6.1). We then consider how the aforementioned observational characteristics of SN 2012fr inform us about the probable nature of its explosion (Section 6.2). Finally we consider the viability of SN 2012fr as a fundamental calibrator for measuring the Hubble constant (Section 6.3).

6.1. SN 2012fr and Velocity Evolution of Other SNe Ia

One of the most noteworthy features of the spectra of SN 2012fr was the extremely clear distinction between the low velocity photospheric Si II $\lambda 6355$ and a higher velocity feature (HVF). Clear identification of two absorption minima in the Si II $\lambda 6355$ line has only been previously observed convincingly in SN 2009ig (Marion 2013), but HVFs may manifest more subtly in the line profiles of other SNe Ia. This may then have an impact on the measurement of the Si II $\lambda 6355$ line velocity.

To inspect how common early HVF behavior is in SNe Ia, we searched for SNe Ia with spectra similar to the -10 day spectrum of SN 2012fr by employing the supernova identification (SNID – Blondin & Tonry 2007) code. The top matches were, as expected, spectra of SNe Ia at about 10 days before maximum light, many of which exhibited a broad boxy absorption profile in the Si II $\lambda 6355$ line. In Figure 18 we plot the Si II $\lambda 6355$ profile of three notable matches – SN 2009ig (Foley et al. 2012; Marion 2013), SN 2007le (from Blondin et al. 2012), and SN 2005cf (Wang et al. 2009b) – all of which exhibit an absorption line profile which seems difficult to explain with a single absorption profile, either Gaussian or P-Cygni. The Si II $\lambda 6355$ profile shape is best explained by a two component profile like that observed in SN 2012fr,

and this probability has been noted by previous authors (Mazzali 2001; Wang et al. 2009b; Foley et al. 2012).

A possible consequence of early high velocity features in SNe Ia could be an over-estimation of the velocity gradient in the Si II $\lambda 6355$ line. To test this possibility, we convolved our spectra of SN 2012fr with a Gaussian filter of width $\sigma = 2500 \text{ km s}^{-1}$ (FWHM $\sim 5600 \text{ km s}^{-1}$) and measured the velocity minimum of the Si II $\lambda 6355$ line. During the early epochs when the Si II $\lambda 6355$ HVF is clearly distinct in the observed spectra, our convolved spectra show a single broad absorption feature whose velocity smoothly declines from $v \sim 22,000 \text{ km s}^{-1}$ to $v \sim 12,000 \text{ km s}^{-1}$ over about 6 days (velocities were almost exactly the pEW-weighted mean of the velocities from Table 3).

Though this implied velocity gradient is much higher than that observed in any other SNe Ia, it illustrates the fact that multiple distinct components blended in velocity space could masquerade as a single rapidly evolving component. Inspection of the shape of the Si II $\lambda 6355$ absorption profile in HVG SNe Ia may provide insight into the possible impact of high velocity features on the measured velocity gradients of these SNe.

Finally, we note that the long velocity plateau observed in SN 2012fr may not be unique, but instead may have been missed in other SNe Ia where the Si II $\lambda 6355$ line is blended with the neighboring Fe lines at late times. Inspection of the full line complex in spectra later than +20 days (see Figure 1) shows the mean wavelength of the absorption lines near Si II $\lambda 6355$ becomes redder, due to multiple Fe lines appearing to the red of Si II $\lambda 6355$, while the individual lines remain at constant velocity. This behavior may be hidden in other SNe Ia with broader lines, or may be misinterpreted as a decrease in the line velocity. Indeed, our test of the velocity-broadened spectra of SN 2012fr revealed a slight decrease in the broadened velocity minimum starting at about +20 days. Future modeling of the SN 2012fr spectra released here may be able to address this question in more detail by identifying the neighboring lines to Si II $\lambda 6355$ and how their relative strengths evolve with time.

6.2. The nature of the SN 2012fr explosion

The key observational features of SN 2012fr – long Si and Ca velocity plateau, narrow absorption features, and early high velocity features (HVFs) – provide critical clues to the nature of its explosion. We will argue here that these observations indicate a thin region of partial burning products which produce the observed narrow line widths and IME velocity plateau, and which may be indicative of stratification in the ejecta. We then speculate on the origin of the HVFs, particularly in context of recent proposals for surface He shell burning.

6.2.1. Ejecta Stratification

The narrow velocity width of the absorption profiles in SN 2012fr have enabled us to unambiguously track the velocity of the Si II $\lambda 6355$ to very late times, revealing a velocity plateau at $v \sim 12,000 \text{ km s}^{-1}$ until at least the final epoch of observation at +39 days. SNe Ia with such low velocity gradients have been observed before (e.g. the “LVG” subclass from Benetti et al. 2005). Notably, several SNe Ia have been noted to exhibit a

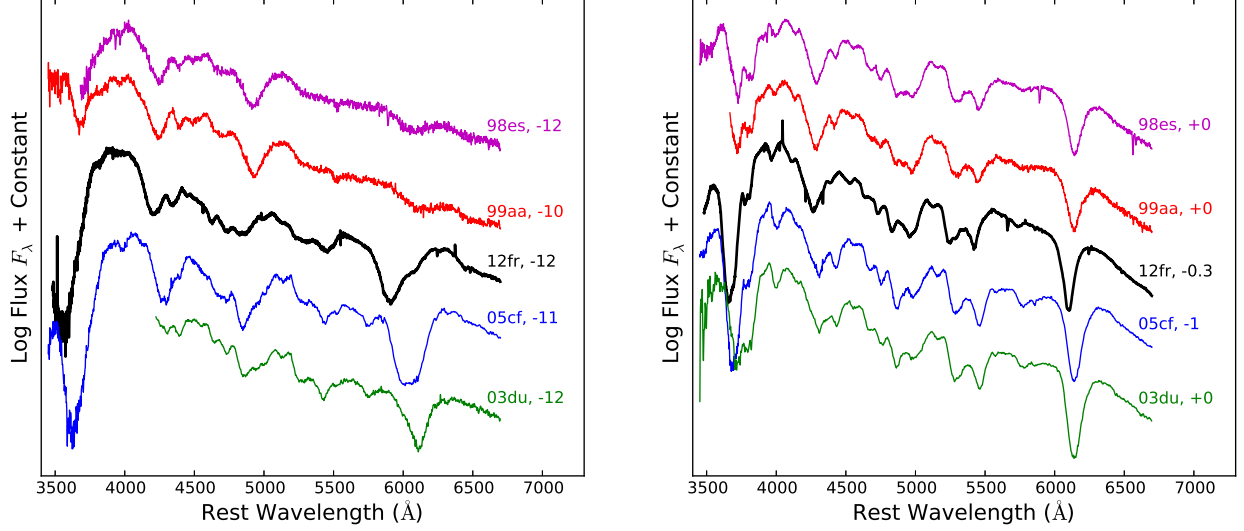


Figure 17. Spectrum of SN 12fr compared to other SNe Ia at ~ 12 days before maximum light (left) and at maximum light (right). Comparison SNe Ia are the SN 1991T-like SN 1998es (from Blondin et al. 2012), SN 1999aa (from Blondin et al. 2012), and the normal SNe Ia SN 2005cf (Wang et al. 2009b) and SN 2003du (Stanishev et al. 2007).

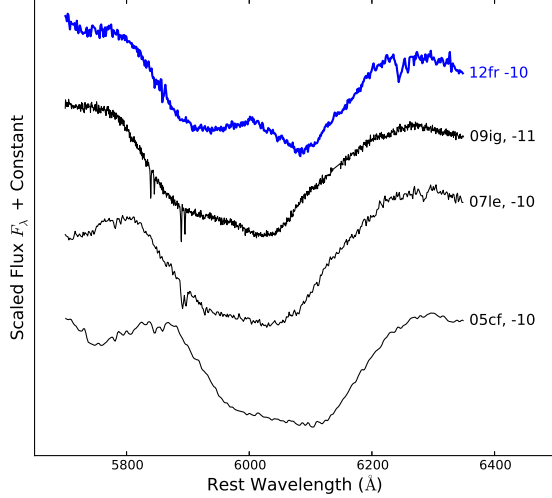


Figure 18. Si II $\lambda 6355$ feature in the -10 day spectrum of SN 12fr (blue) vs. early spectra of other SNe Ia with likely Si II $\lambda 6355$ HVFs: SN 2009ig (Foley et al. 2012; Marion 2013), SN 2007le (from Blondin et al. 2012), and SN 2005cf (Wang et al. 2009b).

short-lived (i.e. few weeks duration) velocity plateau, such as the super-Chandrasekhar candidates presented in Scalzo et al. (2012), as well as SN 2005hj (Quimby et al. 2007) which also demonstrated narrow velocity width.

The velocity plateaus for these other SNe Ia were explained in terms of explosion models featuring density enhancements at a particular velocity, which form at the reverse shock of an interaction between the SN ejecta and overlying material. Examples include “tamped detonations” and “pulsating delayed detonations”, such as the DET2ENV and PDD series models of Khokhlov et al. (1993). In a tamped detonation, the SN ejecta interact with a compact envelope of H-poor material, such as

the carbon/oxygen envelope which might remain after a double-degenerate merger (Fryer et al. 2010; Shen et al. 2012); the interaction freezes out quickly and the shock structure expands homologously thereafter. In a pulsating delayed detonation, the initial deflagration phase quenches and the white dwarf progenitor undergoes a strong pulsation, causing the outer layers to contract. The contraction then re-ignites carbon and eventually results in a transition to a detonation, in which a shock forms at the interface between the expanding inner layers and contracting outer layers.

Regardless of how it forms, the dense layer in these models remains optically thick for some time, resulting in a plateau in the Si II velocity. Our analysis of Fe II lines in SN 12fr, however, suggests that Si II detaches from the photosphere between day +8 and day +11, disfavoring a pure density enhancement as the cause of the Si II plateau in SN 12fr. Additionally, in a tamped detonation one would expect that material above the density-enhanced layer would correspond primarily to the unburned envelope; thus the Si II HVF we observe in SN 12fr is difficult to explain in this scenario.

Rather than indicating a pure density enhancement, the velocity plateau in Si II $\lambda 6355$ may be evidence of Si II being confined to a narrow region in velocity space. This possibility is reinforced by the analogous velocity plateau in the Ca II IR triplet (Section 4.3.1) as well as the slightly lower velocity of the Fe II lines at late times (Section 4.4). This layering, along with the narrowness of the absorption features, indicate a probable stratification of the progress to complete nuclear burning in the ejecta. These properties are common in scenarios where the intermediate mass elements are mainly produced in a detonation phase (see e.g. the recent work by Seitenzahl et al. 2013) as compared to deflagration scenarios, which result in significantly increased mixing in the ejecta.

Corroboration of stratification in the ejecta of

SN 2012fr will be aided by nebular spectroscopy. Specifically, if the IMEs are distributed in a spherically symmetric shell, these should manifest as double peaked nebular lines such as the argon lines astutely observed by Gerardy et al. (2007) in the mid-IR nebular spectrum of SN 2005df. Conversely, if the IMEs are distributed asymmetrically, as discerned from spectropolarimetric observations by Maund et al. (2013), this may be revealed in asymmetry of the nebular IME line profile (unless of course the asymmetric geometry is not oriented favorably). However, IME nebular lines are challenging to observe and most lines in nebular spectra arise from material burned to full nuclear statistical equilibrium (Fe and Ni). As Maund et al. (2013) note, a global asymmetry of SN 2012fr would manifest as a velocity shift of the nebular Fe lines, following the prediction of Maeda et al. (2010).

6.2.2. High Velocity Features

The high-velocity features (HVF) in both silicon and calcium also shed light on the nature of the SN 2012fr explosion. HVFs in the Ca II IR triplet appear to be a very common, perhaps even ubiquitous, feature in early SN Ia spectra (e.g. Mazzali et al. 2005b). HVFs in the Si II $\lambda 6355$ have also been observed in many SNe Ia (e.g. Wang et al. 2009b; Foley et al. 2012; Blondin et al. 2012; Silverman et al. 2012a; Marion 2013). Positive identification of HVFs in other lines has been a more challenging effort (though see Marion 2013, for a thorough inspection of HVFs in multiple atomic species for SN 2009ig), so much effort has been focused on investigating the Ca II IR triplet and Si II $\lambda 6355$ HVFs. Both the geometric distribution and physical origin of the material responsible for these HVFs are active areas of investigation.

Tanaka et al. (2006) posited that the HVFs are due to patches of material outside the nominal photosphere, and that the relative strength of the photospheric and HV features was due to the relative “covering fraction” of the outer layer of material. If the HVFs originated from patchy layers of material, they would likely lack spherical symmetry. Maund et al. (2013) recently presented spectropolarimetry observations of SN 2012fr and argued that the relatively high degree of polarization in the HVFs is inconsistent with spherically symmetric geometry. Such asymmetry in HVFs has been inferred from spectropolarimetric observations of other SNe Ia as well (for a review see Wang & Wheeler 2008).

The physical origin of HVF material remains unclear. It has been suggested that HVFs could be due to circum-stellar material (CSM – Gerardy et al. 2004; Mazzali et al. 2005a), and for some SNe Ia CSM models have yielded favorable agreement with early SN Ia spectra with HVFs (Altavilla et al. 2007; Tanaka et al. 2008). In this scenario, absorption by Si II and Ca II may be enhanced if the CSM is partially enriched in hydrogen (CSM with $X(H) < 0.3$ would not produce a detectable H α feature – Tanaka et al. 2008), thereby favoring a lower ionization state for these ions. However, significant absorption by Ca and Si across a range of velocities in SN 2012fr is indicative of these features being produced by material in (or on) the WD that undergoes partial nuclear burning during (or prior to) the supernova explosion.

A possible explanation for the HVFs in SN 2012fr may

be the detonation of He-rich material at the surface of the exploding WD. If a He layer of sufficiently low density is consumed by a detonation, the low density prevents burning to Fe group elements but can be sufficient to produce Si and Ca (K. Nomoto, priv. comm.). In the single-degenerate Chandrasekhar-mass scenario, a He layer may be present following accretion from a binary companion. Explosive burning in a surface helium layer is also a generic feature in the double-detonation scenario (Fink et al. 2007, 2010; Kromer et al. 2010; Sim et al. 2010, 2012), where the detonation of the helium layer induces a detonation near the core of the WD progenitor, and even in merger scenarios in which the CO WDs retain a small He-rich atmosphere (R. Pakmor, priv. comm.). Recent work by Townsley et al. (2012) showed that helium shell burning could produce significant amounts of calcium, especially if the surface layer dredges up carbon from the white dwarf surface through convection. However, one drawback of the He shell scenario is that significant amounts of unburned helium remain in most simulations, and while the remaining helium should produce clear signatures in SN Ia spectra (Mazzali & Lucy 1998) these features are not observed in SNe Ia.

Another possibility is that Si and Ca abundances are enhanced in the outer layers of a WD due to surface He burning that occurred prior to the supernova event. This might arise during a surface He flash (e.g. Nomoto et al. 2013) which might manifest observationally as a recurrent nova. This He shell flash could produce relatively high Si and Ca abundances in the outer layers of the WD, or might also ejecta partial burning products. These might either fall back onto the surface of the WD (again providing enrichment of the outer WD layers prior to explosion), or perhaps could enrich part of the CSM into which the supernova eject subsequently expand, and in principle the ejected material might be directly detected as CSM interaction of the SN (e.g. as in PTF11kx – Dilday et al. 2012).

Thus it is difficult at this time to constrain the exact origin of HVFs in SNe Ia, including in SN 2012fr, but our data provide important observational constraints. HVFs in both Si II $\lambda 6355$ and the Ca II IR triplet were observed from two weeks before maximum light until they faded to obscurity at roughly -2 and +10 days, respectively. These HVFs were cleanly distinguished from the thin photospheric shell, and showed strong velocity gradients consistent with a receding photosphere. The velocity and absorption strength evolution of these HVFs, along with the geometry implied from spectropolarimetry (Maund et al. 2013), provide important constraints for any model which posits an explanation for these features.

6.3. SN 2012fr as a fundamental calibrator for measuring the Hubble constant

SN 2012fr occurred in NGC 1365, one of the galaxies included in the *HST* Key Project on the extragalactic distance scale (Freedman et al. 2001; Silbermann et al. 1999). This fortuity has made it a leading candidate to contribute toward measurement of the *absolute* luminosity of SNe Ia. Such measurements are critical for measuring the Hubble constant, and in the recent H_0 measurement by Riess et al. (2011) only eight SNe Ia

with good light curves had independent distance measurements from Cepheid variable observations in their host galaxies. Due to the existing Cepheid data for NGC 1365, SN 2012fr stands poised to be added to this sample. In this section we inspect the “normality” of SN 2012fr, as well as existing and probable future members of the Hubble constant sample, in order to assess where these fundamental calibrators for cosmology sit in the context of new spectroscopic classification schemes. We will also revisit this topic in further detail in Paper IV (Tucker et al., 2013, in prep.).

In Table 7 we summarize the light curve decline rate and spectroscopic indicator data for the current sample of H_0 calibrators from Riess et al. (2011), as well as a sample of seven additional SNe Ia which are strong candidates to be added to the H_0 sample, along with SN 2012fr. Selection criteria for the “likely” sample include: (i) low reddening of the SN from its host, i.e. $A_V \lesssim 0.5$, (ii) high sampling of the SN light curve including pre-maximum data, (iii) no spectroscopic peculiarity of the SN, (iv) distance modulus of the host of $\mu \lesssim 32.8$, and (v) low enough inclination to avoid crowding of Cepheids (L. Macri, A. Riess, priv. comm.). The seven new SNe Ia which likely satisfy these criteria are SN 1998dh, SN 2001el, SN 2003du, SN 2005cf, SN 2006D, SN 2009ig, and SN 2011fe.

In Figure 19 we plot the location of existing and likely future H_0 calibrator SNe Ia along with SN 2012fr and the same comparison sample from Figure 16. The H_0 calibrator sample is not composed exclusively of SNe Ia falling in the “core normal” spectroscopic class of Branch et al. (2009) or the “normal” velocity class of Wang et al. (2009a). SN 2012fr would have the slowest light curve decline rate and shallowest silicon absorption of the H_0 sample, but not the highest velocity. Inclusion of SN 2012fr in the H_0 sample will broaden the parameter space coverage of normal SNe Ia used in measuring the Hubble constant.

7. CONCLUSIONS

We presented optical spectra of SN 2012fr, a relatively normal Type Ia supernova which exhibited several interesting features. These include the distinct presence of high velocity features in both the Si II $\lambda 6355$ line and Ca II IR triplet, as well as a long-lived velocity plateau at late epochs in both lines. These behaviors were made more clear by the extremely narrow velocity width of the photospheric absorption line profiles. We showed that SN 2012fr has Si II velocities and absorption strengths which place it near the boundary between the “shallow silicon” and “core normal” spectroscopic classes defined by Branch et al. (2009), and on the boundary between normal and “high velocity” SNe Ia as defined by Wang et al. (2009a).

SN 2012fr exhibited a very slow decline rate ($\Delta m_{15}(B) = 0.80 \pm 0.01$ – see Paper I), relatively shallow silicon absorption at maximum light ($pEW(6355) = 66.5 \pm 15.5$), and a very low velocity gradient ($\dot{v} = 0.3 \pm 10.0$). All of these characteristics are common in the very luminous SN 1991T-like and SN 1999aa-like SN Ia sub-classes, but SN 2012fr has higher ejecta velocities and much stronger Si and Ca absorption at early epochs than most SNe Ia in these classes (see Figure 17). Thus SN 2012fr likely represents the most luminous end of the

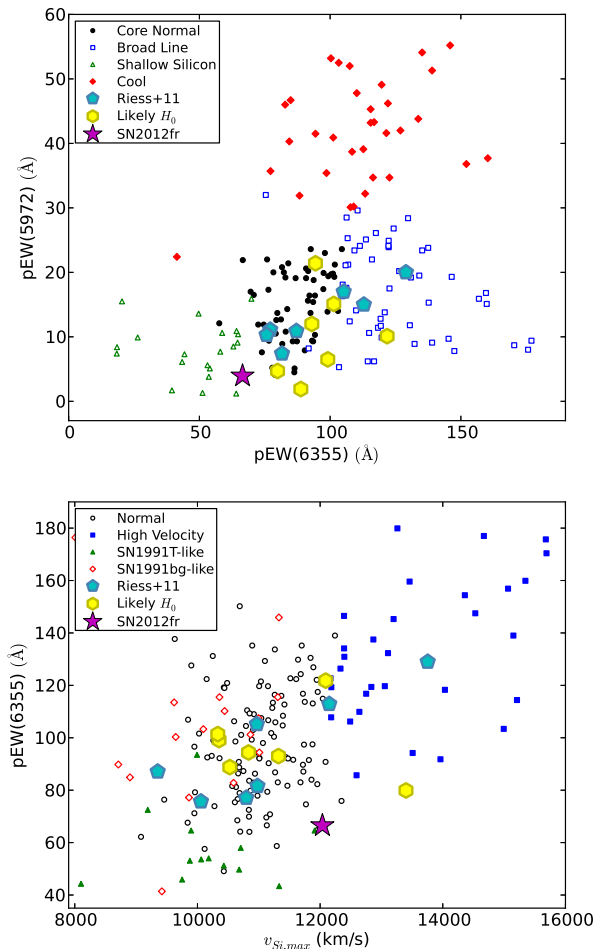


Figure 19. Current members of the H_0 fundamental calibrator sample (cyan pentagons) and likely new additions to the sample (yellow hexagons), along with SN 2012fr (purple star), compared to other SNe Ia on the Branch et al. (2009) diagram (top) and Wang et al. (2009a) diagram (bottom). Other SN Ia subclasses are denoted as in Figure 16.

normal SN Ia spectrum, and may be a transitional object between normal and very luminous events.

In the modern era only three well-observed normal SNe Ia (SN 1981B, SN 2001el, SN 2011fe) have occurred in galaxies that are both suitable for Cepheid distances and closer than the host galaxy of SN 2012fr, NGC 1365. Furthermore, this galaxy has been extensively studied and was part of the *HST* Key Project on the extragalactic distance scale. This makes SN 2012fr a prime candidate for measuring the absolute luminosity of SNe Ia and thereby constraining the Hubble constant, and we showed that SN 2012fr would provide an excellent complement to the existing and likely future sample of H_0 SNe Ia.

Individual SNe Ia such as SN 2012fr with extensive observational data sets can prove invaluable for better understanding the nature of SN Ia explosions. Here we already identified a number of tantalizing observational characteristics of this spectral time series, and expect

Table 7
Spectroscopic Classes of H_0 Fundamental Calibrators

SN	Host	D ^a (Mpc)	$\Delta m_{15}(B)$	$pEW(5972)$ (Å)	$pEW(6355)$ (Å)	v_{Si} (km/s)	Branch Class	Wang Class	References
SN1981B	NGC 4536	14.8	1.07 ± 0.09	20.0	129.0	13754	BL	HV	1,2,3
SN1990N	NGC 4639	21.6	1.00 ± 0.03	10.9	87.1	9352	CN	N	4,5
SN1994ae	NGC 3370	26.6	0.96 ± 0.04	7.4	81.6	10979	CN	N	5
SN1995al	NGC 3021	30.5	0.87 ± 0.04	15.0	112.9	12149	BL	HV	5
SN1998aq	NGC 3982	22.5	1.11 ± 0.04	11.1	77.1	10796	CN	N	5
SN2002fk	NGC 1309	32.5	1.13 ± 0.03	10.3	75.7	10057	CN	N	5
SN2007af	NGC 5584	22.4	1.04 ± 0.01	17.0	105.2	10969	BL	N	5
SN2007sr	NGC 4038	21.7	1.13 ± 0.06	6
SN1998dh	NGC 7541	36.7	1.17 ± 0.06	10.1	121.8	12091	BL	HV	5
SN2001el	NGC 1448	15.9	1.13 ± 0.04	12.0	93.0	11321	CN	N	7,8
SN2003du	UGC 9391	26.1	1.07 ± 0.06	1.9	88.8	10527	CN	N	5,9
SN2005cf	MCG -01-39-3 ^b	26.4	1.05 ± 0.03	6.5	99.1	10352	CN	N	10,5
SN2006D	MCG -01-33-34	34.9	1.35 ± 0.05	21.4	94.4	10833	CN	N	5
SN2009ig	NGC 1015	35.9	0.89 ± 0.02	4.7	79.9	13400	CN	HV	11, 12, 5
SN2011fe	M101	6.7	1.07 ± 0.06	15.1	101.4	10331	CN	N	13, 14
SN2012fr	NGC 1365	17.9	0.80 ± 0.01	3.9	66.5	12037	SS/CN	HV/N	—

^a Distances from Cepheids for Riess et al. (2011) sample, Kennicutt et al. (1998) and Freedman et al. (2001) for M101, Silbermann et al. (1999) and Freedman et al. (2001) for NGC 1365, from redshift using $H_0 = 73.8$ km/s Mpc⁻¹ for others.

^b Tidal bridge between MCG -01-39-3 and MCG -01-39-2 (NGC 5917) - see Wang et al. (2009b).

References: (1) Schaefer (1995), (2) Branch et al. (1983), (3) Branch et al. (2009), (4) Ganeshalingam et al. (2010), (5) Blondin et al. (2012), (6) Hicken et al. (2012), (7) Krisciunas et al. (2003), (8) Wang et al. (2003), (9) Stanishv et al. (2007), (10) Wang et al. (2009b), (11) Foley et al. (2012), (12) Marion (2013), (13) Vinkó et al. (2012), (14) Parrent et al. (2012)

that future detailed modeling could reveal even subtler insights.

Facilities: ANU:2.3m (WiFeS), NTT (EFOSC2), NTT (SOFI), SALT (RSS), SAAO:1.9m (Grating Spectrograph), Shane (Kast Double spectrograph), Keck:I (HIRES)

Acknowledgments: We are very grateful to the staff of RSAA and Siding Spring Observatory for their rapid replacement of a broken cooling pump for the WiFeS red channel on November 1st, particularly Graeme Blackman, Gabe Bloxham, Donna Burton, Harvey Butcher, Mike Ellis, Mike Fowler, Mike Petkovic, Annino Vaccarella, and Peter Verwayen.

We thank Bruce Bassett for arranging observations with the SAAO 1.9m telescope. We thank Carl Melis, Michael Jura, Siyi Xu, Beth Klein, Ben Zuckerman, and Tim Pickering for contributing data. We thank Stephane Blondin for providing his velocity gradient values for the CfA SN Ia sample. We are grateful to Ken Nomoto, Rudiger Pakmor, Lucas Macri, and Adam Riess for helpful discussions. We also thank Howie Marion for providing an advance copy of his paper on SN 2009ig, and for very helpful discussions.

This research was conducted by the Australian Research Council Centre of Excellence for All-sky Astrophysics (CAASTRO), through project number CE110001020. Chris Lidman is the recipient of an Australian Research Council Future Fellowship (program number FT0992259). J. A. acknowledges support by CONICYT through FONDECYT grant 3110142, and by the Millennium Center for Supernova Science (P10-064-F), with input from 'Fondo de Innovación para la Competitividad, del Ministerio de Economía, Fomento y Turismo de Chile'. AGY is supported by the EU/FP7 via an ERC grant. F.B. acknowledges support from FONDECYT through Postdoctoral grant 3120227 and from the Millennium Center for Supernova Science through grant P10-064-F (funded by "Programa Bicentenario de Ciencia y Tecnología de CONICYT" and "Programa Iniciativa Científica Milenio de MIDEPLAN"). G.P. acknowledges support from the Millennium Center for Supernova Science through grant P10-064-F funded by "Programa Bicentenario de Ciencia y Tecnología de CONICYT" and "Programa Iniciativa Científica Milenio de MIDEPLAN". S.B. is partially supported by the PRIN-INAF 2011 with the project "Transient Universe: from ESO Large to PESSTO". Support for this research at Rutgers University was provided in part by NSF CAREER award AST-0847157 to SWJ. Some of the observations reported in this paper were obtained with the Southern African Large Telescope (SALT), with proposal ID 2012-1-RU-005 (PI: Jha). M. D. S. and F. T. acknowledge the generous support provided by the Danish Agency for

Science and Technology and Innovation through a Sapere Aude Level 2 grant. E.Y.H is supported by the National Science Foundation under Grant No. AST-1008343.

This work is based in part on observations collected at the European Organisation for Astronomical Research in the Southern Hemisphere, Chile as part of PESSTO, (the Public ESO Spectroscopic Survey for Transient Objects Survey) ESO program 188.D-3003 and program 089.D-0305. This paper uses observations made at the South African Astronomical Observatory (SAAO). Some of the data presented herein were obtained at the W. M. Keck Observatory, which is operated as a scientific partnership among the California Institute of Technology, the University of California, and NASA; the observatory was made possible by the generous financial support of the W. M. Keck Foundation.

This research has made use of the CfA Supernova Archive, which is funded in part by the National Science Foundation through grant AST 0907903. This research has made prodigious use of the NASA/IPAC Extragalactic Database (NED) which is operated by the Jet Propulsion Laboratory, California Institute of Technology, under contract with the National Aeronautics and Space Administration. This research has made use of NASA's Astrophysics Data System (ADS). This work also utilized the Central Bureau for Astronomical Telegrams (CBAT) list of supernovae (<http://www.cbat.eps.harvard.edu/lists/Supernovae.html>).

REFERENCES

- Altavilla, G., et al. 2007, *A&A*, 475, 585
 Benetti, S., et al. 2004, *MNRAS*, 348, 261
 —. 2005, *ApJ*, 623, 1011
 Blondin, S., & Tonry, J. L. 2007, *ApJ*, 666, 1024
 Blondin, S., et al. 2012, *AJ*, 143, 126
 Bongard, S., Baron, E., Smadja, G., Branch, D., & Hauschildt, P. H. 2006, *ApJ*, 647, 513
 Branch, D., Dang, L. C., & Baron, E. 2009, *PASP*, 121, 238
 Branch, D., Lacy, C. H., McCall, M. L., Sutherland, P. G., Uomoto, A., Wheeler, J. C., & Wills, B. J. 1983, *ApJ*, 270, 123
 Branch, D., et al. 2004, *ApJ*, 606, 413
 Buil, C. 2012, *Central Bureau Electronic Telegrams*, 3275, 3
 Bureau, M., Mould, J. R., & Staveley-Smith, L. 1996, *ApJ*, 463, 60
 Buzzoni, B., et al. 1984, *The Messenger*, 38, 9
 Childress, M., Zhou, G., Tucker, B., Bayliss, D., Scalzo, R., Yuan, F., & Schmidt, B. 2012, *Central Bureau Electronic Telegrams*, 3275, 2
 Chotard, N., et al. 2011, *A&A*, 529, L4+

- Crawford, S. M., et al. 2010, in Society of Photo-Optical Instrumentation Engineers (SPIE) Conference Series, Vol. 7737, Observatory Operations: Strategies, Processes, and Systems III. Edited by Silva, David R.; Peck, Alison B.; Soifer, B. Thomas.
- Dilday, B., et al. 2012, *Science*, 337, 942
- Dopita, M., Hart, J., McGregor, P., Oates, P., Bloxham, G., & Jones, D. 2007, *Ap&SS*, 310, 255
- Dopita, M., et al. 2010, *Ap&SS*, 327, 245
- Filippenko, A. V., et al. 1992, *ApJ*, 384, L15
- Fink, M., Hillebrandt, W., & Röpke, F. K. 2007, *A&A*, 476, 1133
- Fink, M., Röpke, F. K., Hillebrandt, W., Seitenzahl, I. R., Sim, S. A., & Kromer, M. 2010, *A&A*, 514, A53
- Folatelli, G., et al. 2012, *ApJ*, 745, 74
- Foley, R. J. 2012, *ArXiv e-prints*
- Foley, R. J., Sanders, N. E., & Kirshner, R. P. 2011, *ApJ*, 742, 89
- Foley, R. J., et al. 2012, *ApJ*, 744, 38
- Freedman, W. L., et al. 2001, *ApJ*, 553, 47
- Fryer, C. L., et al. 2010, *ApJ*, 725, 296
- Ganeshalingam, M., et al. 2010, *ApJS*, 190, 418
- Garavini, G., et al. 2004, *AJ*, 128, 387
- Gerardy, C. L., et al. 2004, *ApJ*, 607, 391
- . 2007, *ApJ*, 661, 995
- Hicken, M., et al. 2012, *ApJS*, 200, 12
- Hsiao, E. Y., et al. 2013, *arXiv:1301.6287*
- Kennicutt, Jr., R. C., et al. 1998, *ApJ*, 498, 181
- Khokhlov, A., Mueller, E., & Hoefflich, P. 1993, *A&A*, 270, 223
- Klotz, A., Normand, J., Conseil, E., Parker, S., Fabrega, J., & Maury, A. 2012, *Central Bureau Electronic Telegrams*, 3276, 1
- Krisciunas, K., et al. 2003, *AJ*, 125, 166
- Kromer, M., Sim, S. A., Fink, M., Röpke, F. K., Seitenzahl, I. R., & Hillebrandt, W. 2010, *ApJ*, 719, 1067
- Maeda, K., et al. 2010, *Nature*, 466, 82
- Maguire, K., et al. 2012, *MNRAS*, 426, 2359
- Marion, G. H. 2013, in prep.
- Matheson, T., et al. 2008, *AJ*, 135, 1598
- Maund, J. R., et al. 2013, *arXiv:1302.0166*
- Mazzali, P. A. 2001, *MNRAS*, 321, 341
- Mazzali, P. A., Benetti, S., Stehle, M., Branch, D., Deng, J., Maeda, K., Nomoto, K., & Hamuy, M. 2005a, *MNRAS*, 357, 200
- Mazzali, P. A., & Lucy, L. B. 1998, *MNRAS*, 295, 428
- Mazzali, P. A., Nomoto, K., Cappellaro, E., Nakamura, T., Umeda, H., & Iwamoto, K. 2001, *ApJ*, 547, 988
- Mazzali, P. A., Röpke, F. K., Benetti, S., & Hillebrandt, W. 2007, *Science*, 315, 825
- Mazzali, P. A., et al. 2005b, *ApJ*, 623, L37
- Miller, J. S., & Stone, R. P. S. 1993, *Lick Obs. Tech. Rep.* 66 (Santa Cruz: Lick Obs.)
- Moorwood, A., Cuby, J.-G., & Lidman, C. 1998, *The Messenger*, 91, 9
- Nomoto, K., Kamiya, Y., & Nakasato, N. 2013, in *IAU Symposium*, Vol. 281, *IAU Symposium*, 253–260
- Nugent, P., Phillips, M., Baron, E., Branch, D., & Hauschildt, P. 1995, *ApJ*, 455, L147
- Nugent, P. E., et al. 2011, *Nature*, 480, 344
- Parrent, J. T., et al. 2011, *ApJ*, 732, 30
- . 2012, *ApJ*, 752, L26
- Patat, F., et al. 2007, *Science*, 317, 924
- Perlmutter, S., et al. 1999, *ApJ*, 517, 565
- Phillips, M. M. 1993, *ApJ*, 413, L105
- Phillips, M. M., Lira, P., Suntzeff, N. B., Schommer, R. A., Hamuy, M., & Maza, J. 1999, *AJ*, 118, 1766
- Phillips, M. M., Wells, L. A., Suntzeff, N. B., Hamuy, M., Leibundgut, B., Kirshner, R. P., & Foltz, C. B. 1992, *AJ*, 103, 1632
- Pinto, P. A., & Eastman, R. G. 2000, *ApJ*, 530, 757
- Poznanski, D., Ganeshalingam, M., Silverman, J. M., & Filippenko, A. V. 2011, *MNRAS*, 415, L81
- Poznanski, D., Prochaska, J. X., & Bloom, J. S. 2012, *MNRAS*, 426, 1465
- Quimby, R., Höflich, P., & Wheeler, J. C. 2007, *ApJ*, 666, 1083
- Riess, A. G., et al. 1998, *AJ*, 116, 1009
- . 2011, *ApJ*, 730, 119
- Scalzo, R., et al. 2012, *ApJ*, 757, 12
- Schaefer, B. E. 1995, *ApJ*, 449, L9
- Schlafly, E. F., & Finkbeiner, D. P. 2011, *ApJ*, 737, 103
- Seitenzahl, I. R., et al. 2013, *MNRAS*, 429, 1156
- Shen, K. J., Bildsten, L., Kasen, D., & Quataert, E. 2012, *ApJ*, 748, 35
- Silbermann, N. A., et al. 1999, *ApJ*, 515, 1
- Silverman, J. M., & Filippenko, A. V. 2012, *MNRAS*, 425, 1917
- Silverman, J. M., Kong, J. J., & Filippenko, A. V. 2012a, *MNRAS*, 425, 1819
- Silverman, J. M., et al. 2012b, *MNRAS*, 425, 1789
- . 2012c, *ApJ*, 756, L7
- Sim, S. A., Fink, M., Kromer, M., Röpke, F. K., Ruiter, A. J., & Hillebrandt, W. 2012, *MNRAS*, 420, 3003
- Sim, S. A., Röpke, F. K., Hillebrandt, W., Kromer, M., Pakmor, R., Fink, M., Ruiter, A. J., & Seitenzahl, I. R. 2010, *ApJ*, 714, L52
- Simon, J. D., et al. 2009, *ApJ*, 702, 1157
- Stanishev, V., et al. 2007, *A&A*, 469, 645
- Stehle, M., Mazzali, P. A., Benetti, S., & Hillebrandt, W. 2005, *MNRAS*, 360, 1231
- Sternberg, A., et al. 2011, *Science*, 333, 856
- Tanaka, M., Mazzali, P. A., Maeda, K., & Nomoto, K. 2006, *ApJ*, 645, 470
- Tanaka, M., et al. 2008, *ApJ*, 677, 448
- Thomas, R. C., Nugent, P. E., & Meza, J. C. 2011a, *PASP*, 123, 237
- Thomas, R. C., et al. 2007, *ApJ*, 654, L53
- . 2011b, *ApJ*, 743, 27
- Townsley, D. M., Moore, K., & Bildsten, L. 2012, *ApJ*, 755, 4
- van Rossum, D. R. 2012, *arXiv:1208.3781*
- Vinkó, J., et al. 2012, *A&A*, 546, A12
- Vogt, S. S., et al. 1994, in Society of Photo-Optical Instrumentation Engineers (SPIE) Conference Series, Vol. 2198, *Proc. SPIE Instrumentation in Astronomy VIII*, ed. D. L. Crawford & E. R. Craine, 362
- Wang, L., & Wheeler, J. C. 2008, *ARA&A*, 46, 433
- Wang, L., et al. 2003, *ApJ*, 591, 1110
- Wang, X., et al. 2009a, *ApJ*, 699, L139
- . 2009b, *ApJ*, 697, 380
- Yaron, O., & Gal-Yam, A. 2012, *PASP*, 124, 668